Cell Reports

Article

Retroelement decay by the exonuclease XRN1 is a viral mimicry dependency in cancer

Graphical abstract

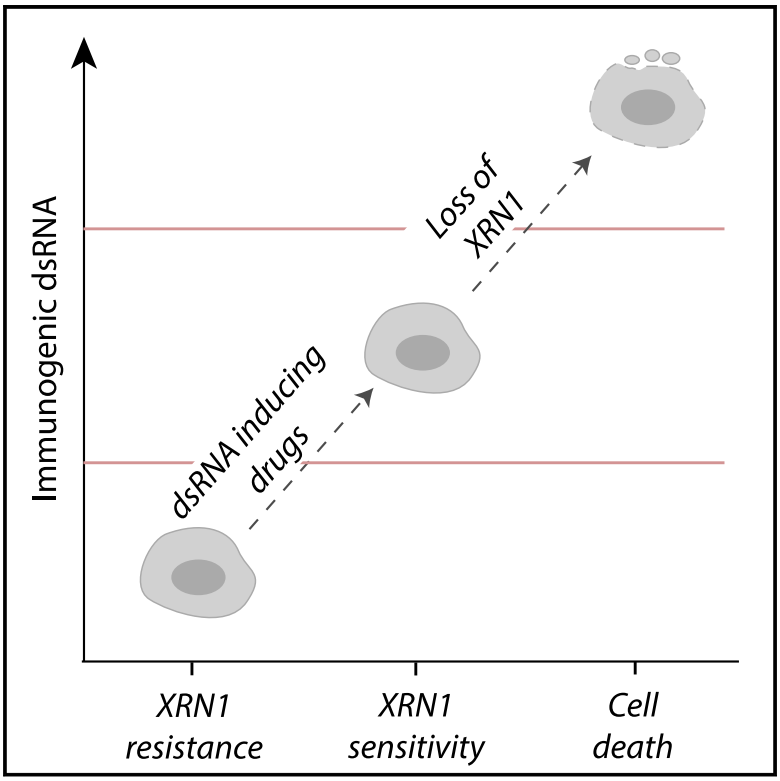

Authors

Amir Hosseini, Håvard T. Lindholm, Raymond Chen, ..., Andrea Di Gioacchino, Benjamin Greenbaum, Daniel D. De Carvalho

Correspondence

daniel.decarvalho@uhnresearch.ca

In brief

Hosseini et al. systematically identify genes protecting cancer cells from cell death from viral mimicry induction. They confirm that loss of the top hit XRN1 leads to cell death in cells with high endogenous dsRNA levels, making XRN1 a potential target for future cancer therapeutics.

Highlights

- Screen for all genes protecting cancer cells from cell death from antiviral state
- XRN1 is a top hit inhibiting cell death from endogenous dsRNA
- Cell lines with high endogenous dsRNA levels are sensitive to XRN1 loss

Hosseini et al., 2024, Cell Reports *43*, 113684
February 27, 2024
https://doi.org/10.1016/j.celrep.2024.113684

CellPress

Cell Reports

CellPress
OPEN ACCESS

Article

Retroelement decay by the exonuclease XRN1 is a viral mimicry dependency in cancer

Amir Hosseini,[1,2,9] Håvard T. Lindholm,[1,3,9] Raymond Chen,[1,4,9] Parinaz Mehdipour,[1,2] Sajid A. Marhon,[1] Charles A. Ishak,[1] Paul C. Moore,[5] Marie Classon,[5] Andrea Di Gioacchino,[6] Benjamin Greenbaum,[7,8] and Daniel D. De Carvalho[1,4,10,*]

[1]Princess Margaret Cancer Centre, University Health Network, Toronto, ON M5G 1L7, Canada
[2]Ludwig Institute for Cancer Research, Nuffield Department of Medicine, University of Oxford, Oxford OX3 7DQ, UK
[3]Department of Pathology, Oslo University Hospital-Rikshospitalet, 0372 Oslo, Norway
[4]Department of Medical Biophysics, University of Toronto, Toronto, ON M5G 1L7, Canada
[5]Pfizer Centers for Therapeutic Innovation, South San Francisco, CA 94080, USA
[6]Laboratoire de Physique de l'Ecole Normale Supérieure, PSL & CNRS UMR8063, Sorbonne Université, Université de Paris, Paris, France
[7]Physiology, Biophysics & Systems Biology, Weill Cornell Medicine, Weill Cornell Medical College, New York, NY 10065, USA
[8]Computational Oncology, Department of Epidemiology and Biostatistics, Memorial Sloan Kettering Cancer Center, New York, NY 10065, USA
[9]These authors contributed equally
[10]Lead contact
*Correspondence: daniel.decarvalho@uhnresearch.ca
https://doi.org/10.1016/j.celrep.2024.113684

SUMMARY

Viral mimicry describes the immune response induced by endogenous stimuli such as double-stranded RNA (dsRNA) from endogenous retroelements. Activation of viral mimicry has the potential to kill cancer cells or augment anti-tumor immune responses. Here, we systematically identify mechanisms of viral mimicry adaptation associated with cancer cell dependencies. Among the top hits is the RNA decay protein XRN1 as an essential gene for the survival of a subset of cancer cell lines. XRN1 dependency is mediated by mitochondrial antiviral signaling protein and protein kinase R activation and is associated with higher levels of cytosolic dsRNA, higher levels of a subset of Alus capable of forming dsRNA, and higher interferon-stimulated gene expression, indicating that cells die due to induction of viral mimicry. Furthermore, dsRNA-inducing drugs such as 5-aza-2′-deoxycytidine and palbociclib can generate a synthetic dependency on XRN1 in cells initially resistant to XRN1 knockout. These results indicate that XRN1 is a promising target for future cancer therapeutics.

INTRODUCTION

When a human cell detects a viral infection, it enters an antiviral state with tailored responses to defeat the infection. For example, the cell will produce interferons (IFNs) that reduce protein synthesis to hinder viral replication, increase the presentation of peptides to the immune system, induce apoptosis, and signal in a paracrine manner to stimulate the same antiviral response in neighboring cells.[1] Interestingly, this antiviral state can also be activated by endogenous stimuli, such as double-stranded RNA (dsRNA) structures derived from endogenous retroelements, in a phenomenon called "viral mimicry."[2–4] Activation of viral mimicry is a promising approach for cancer therapeutics because in the same way the antiviral response can help the body eliminate cells infected with viruses, it can be leveraged to kill cancer cells.[5–8]

Endogenous retroelements are sections of DNA that can duplicate within the genome through an RNA intermediate.[9] In homeostasis, endogenous retroelements are typically repressed through a variety of mechanisms in order to prevent deleterious effects such as genomic instability or inappropriate immune activation. Therapeutic disruption of these mechanisms, such as with the DNA-demethylating agent 5-aza-2′-deoxycytidine (5-AZA-CdR), can lead to retroelement expression and formation of dsRNA structures that bind to innate immune receptors and produce a viral mimicry response.[3–5] Beyond DNA methylation, disruption of histone modifications,[6,10] splicing,[7,11] and RNA editing[5,12–14] have also been implicated in viral-mimicry-mediated anticancer effects. Due to the wide variety of cellular processes involved, we have proposed that in addition to their role in cancer treatment, endogenous retroelements can act as an alarm for disruptions to cellular homeostasis that cull pre-cancerous cells.[15] Despite this, cancers often paradoxically display elevated levels of endogenous retroelements,[2] suggesting that these cancers have developed mechanisms of viral mimicry adaptation. Such mechanisms may represent cancer dependencies that can be targeted therapeutically to resensitize tumors to viral mimicry.

Previously, we identified upregulation of the p150 isoform of the RNA-editing enzyme adenosine deaminase acting on RNA 1 (ADAR1) as one such adaptation.[5] ADAR1 catalyzes adenosine-to-inosine (A-to-I) editing primarily in RNA duplex structures derived from Alus,[16] a family of endogenous retroelements that make up about 10% of the human genome.[17] Adjacent Alus found

on the same strand but in opposite orientations are known as inverted-repeat Alus (IR-Alus) and can form dsRNA hairpin structures when transcribed together.[5] In the absence of ADAR1, IR-Alu dsRNAs are recognized by innate immune receptors such as melanoma differentiation-associated protein 5 (MDA5),[18] which then activates IFN signaling through the mitochondrial antiviral-signaling protein (MAVS) pathway. The subsequent expression of IFN-stimulated genes (ISGs) results in an antiviral cell state. A-to-I editing by ADAR1 creates bulges in the dsRNA structure that prevent MDA5 recognition,[18] allowing cancer cells with upregulated ADAR1 to circumvent viral mimicry activation. However, this ADAR1 dependency provides a vulnerability that can be exploited for cancer therapy. Accordingly, our previous work indicates that depletion of ADAR1 potentiates viral-mimicry-inducing epigenetic therapies.[5]

Here, we systematically screened for other viral mimicry dependencies by correlating ISG expression in cell lines from the Cancer Cell Line Encyclopedia (CCLE) with cell viability after genetic knockout as determined in the DepMap dataset.[19,20] This analysis identified pathways of interest, including RNA modification and nucleic acid metabolism pathways. Among the top hits for individual genes was the RNA decay protein XRN1, which degrades RNA without a 5′ cap in the 5′ to 3′ direction.[21] XRN1 dependency was associated with high basal levels of viral mimicry activation, as determined by dsRNA levels and ISG expression, and was mediated by MAVS and protein kinase R (PKR). Furthermore, while cancer cells with low baseline viral mimicry levels were XRN1 independent, we created a synthetic XRN1 dependency through treatment with drugs that increase dsRNA levels. These results highlight XRN1 as a promising therapeutic target partly independent of ADAR1 and demonstrate the utility of our screening approach, suggesting that validation of other identified hits may reveal additional viral mimicry dependencies.

RESULTS

Identification of genes regulating viral mimicry adaptation

Disruptions to cellular mechanisms are common in cancer and can lead to the presence of immunogenic endogenous retroelements and viral mimicry.[15] To survive this viral mimicry induction, cancer cells depend on adaptation mechanisms such as A-to-I editing of dsRNA by ADAR1 to avoid viral-mimicry-induced cell death.[5] Liu et al. and Gannon et al. have previously used the CCLE and Cancer Dependency Map (DepMap) datasets to identify ADAR1 as a dependency in a subset of cancer cells,[22,23] and here we expand this analysis to systematically detect viral mimicry dependencies. To broadly define viral mimicry activation at baseline in different cancer types, we calculated the average scaled ISG expression for 1,005 human cell lines in the CCLE using a previously published ISG signature.[23] We reasoned that the cell lines with high ISG expression would depend on viral-mimicry-inhibiting genes such as ADAR1 to adapt to the high levels of viral mimicry. To test this hypothesis, we compared ISG induction to the effect of ADAR1 knockout on viability from the DepMap CRISPR dataset in 1,005 cell lines (Figure 1A).[20] We found a significant correlation between ADAR1-knockout-mediated decrease in viability and ISG expression across the cell lines, suggesting that cell lines with high ISG expression depend on ADAR1 to survive the induction of viral mimicry, confirming previous findings.[5,22,23] To search for other viral mimicry adaptation mechanisms, we extended the analysis to the correlation between ISG expression and viability upon individual knockout of all genes (Figures 1B; Table S1). This analysis revealed genes that cancer cells depend on to survive viral mimicry induction and are therefore potential targets for cancer therapeutics. Among the hits, ADAR1 had the highest correlation between ISG expression and the effect on viability. ADAR1 is also the protein with the lowest p value when correlating ISG protein levels and effect of knocking out a gene according to the DepMap dataset (Figures S1A and S1B).

To explore mechanisms of viral mimicry adaptation, we selected the top 50 genes with a negative slope and clustered them with the STRING tool (Figure 1C).[24] Among these 50 genes, we found enrichment of immune activation pathways such as "regulation of immune response" and "regulation of type I IFN-mediated signaling pathway" (Figure 1D). As dsRNA is a common activator of viral mimicry, it is interesting that we found Gene Ontology (GO) terms related to RNA processing such as "mRNA methylation" and "nucleic acid metabolic process." Disruption of RNA methylation has been previously linked to innate immune activation from endogenous retroelements.[12–14]

Since high ISG expression can occur through multiple mechanisms, the correlation between high ISG expression and dependency on a gene could reveal diverse mechanisms for viral mimicry adaptation. To focus our analysis on targets that regulate the presence of immunogenic endogenous retroelements, we also compared the dependency of a gene to the sensitivity to ADAR1 knockout. ADAR1 was the top hit correlating with ISG expression and has been previously shown to inhibit the activation of innate immune receptors by dsRNA from endogenous retroelements and thus viral mimicry.[5] We therefore did a linear regression analysis between sensitivity to ADAR1 knockout and the sensitivity to knockout of other genes and plotted the slope and p value for each correlation (Figure 1E). Among the top 50 downregulated genes, the terms "mRNA metabolic process" and "viral process" were enriched, which is consistent with our previous enrichment of nucleic acid metabolism and immune response pathways (Figures S1C and S1D). Out of all genes, the RNA decay protein XRN1 had the lowest p value and the highest R value (0.471) in the correlation with ADAR1 (Figures 1E and 1F). XRN1 was also among the 50 genes with the lowest p value in both the ISG correlation analysis and the ADAR1 knockout correlation analysis (Figure 1G). Interestingly, when we correlated the effect on the viability of XRN1 knockout with gene expression for all genes, we found that the genes with the lowest p value are enriched with pathways connected to an antiviral state (Figures S1E–S1H; Table S2). Out of the top 50 genes, 31 are part of the GO term "defense response to virus" (Figures S1G and S1H). This analysis demonstrates a correlation between baseline ISG induction and sensitivity to XRN1 depletion (Figure S2A).

XRN1 dependency in cancer cell lines is associated with elevated ISG expression and dsRNA levels

We reasoned that cells with higher baseline dsRNA accumulation would be more dependent on RNA decay proteins such as XRN1. To explore the mechanism of XRN1-dependent adaptation to

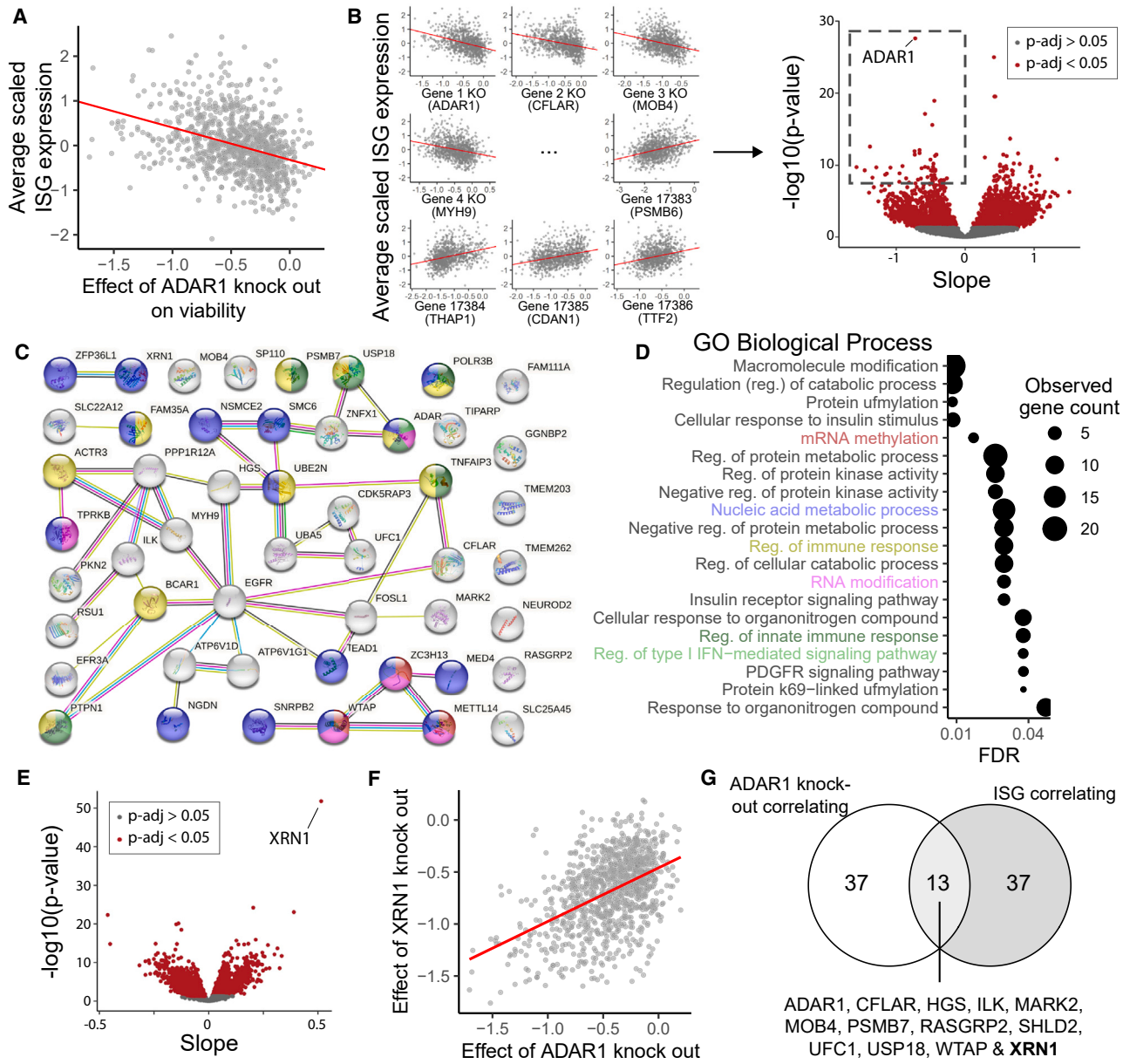

Figure 1. Discovery of genes regulating viral mimicry adaptation

(A) Linear correlation between the effect of ADAR1 knockout on viability from the CRISPR knockout dataset from DepMap and the average scaled expression of ISGs from CCLE. Each dot represents a cell line, n = 1,005. The value on the x axis is the CERES score from DepMap representing the effect size on viability from knocking out ADAR, normalized against a distribution of non-essential and pan-essential genes. The value on the y axis is the mean of *Z* score-normalized log(TPM+1) values from 38 ISGs defined in Liu et al.[23] Negative value is more sensitive to ADAR1 knockout. R = −0.36, Benjamini-Hochberg-corrected p value for linear correlation = 2.4×10^{-28}.

(B) Analysis in (A) extended to all genes with the resulting slopes and Benjamini-Hochberg-corrected p value for each gene plotted in a volcano plot. The square represents the 50 genes with the lowest p value and with a negative slope.

(C) Network from the STRING tool showing the 50 genes with the lowest p value and with a negative slope (area outlined in B).

(D) Enrichment analysis with the STRING tool showing the 20 GO biological process terms with the highest strength value as determined by STRING. The color of GO term names corresponds to the node color seen in (C).

(E) Slope and Benjamini-Hochberg-corrected p value from the linear correlation between the effect on viability from knocking out ADAR1 from the CRISPR knockout DepMap dataset and all other genes.

(F) Linear correlation between the viability effects of XRN1 knockout and ADAR1 knockout in the CRISPR knockout DepMap dataset. R = 0.47, Benjamini-Hochberg-corrected p = 1.8×10^{-52}.

(G) Comparing the top 50 genes by p value with negative slope in (B) with the top 50 genes with positive slope in (E).

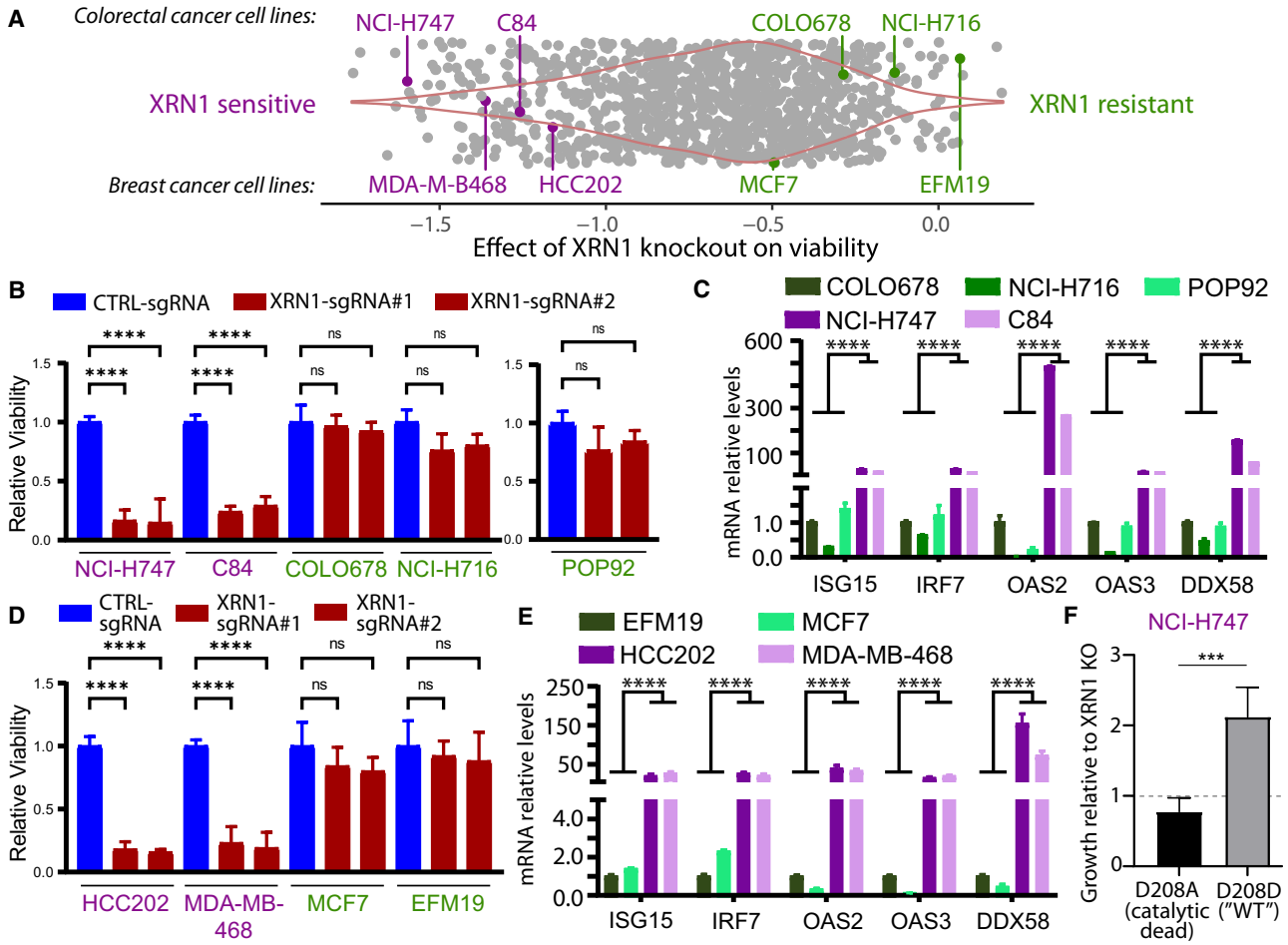

Figure 2. A subset of cancer cell lines are sensitive to XRN1 knockout

(A) Violin plot showing effect on viability from knocking out XRN1 in DepMap data. Selected cell lines are highlighted.

(B) Cell viability assessed by CellTiter-Glo, 5 days after XRN1 knockout with CRISPR-Cas9 in colorectal cancer cell lines. XRN1-sensitive cell lines are colored purple, and XRN1-resistant cell lines are colored green. Data are presented as the mean of duplicates for C84 and of triplicates for other cell lines ±SD. p values were calculated using Bonferroni two-way ANOVA.

(C) qPCR of indicated ISGs in colorectal cancer cells. Values are normalized against RPLP0. Data are presented as the mean of triplicates ±SD. Stars indicate the lowest p value for indicated comparisons. Order of cell lines in bar plot follows order in the legend. p values were calculated using Bonferroni two-way ANOVA.

(D) Same as (B) for breast cancer cell lines.

(E) Same as (C) for breast cancer cell lines.

(F) CRISPR LAPSE of XRN1 D208 mutants in NCI-H747 cells. 7-day fold change of the indicated XRN1 knockin populations after normalizing to matched knockout populations. Data are presented as the mean of six experiments ±SD, and p values were calculated by paired, two-tailed t test.

viral mimicry induction, we used the DepMap dataset to classify cell lines as either XRN1 sensitive (had lower viability after XRN1 knockout) or XRN1 resistant (viability was not affected by XRN1 knockout). We selected two colorectal cancer cell lines (C84 and NCI-H747) and two breast cancer cell lines (HCC202 and MDA-MB-468) that are XRN1 sensitive and two colorectal cancer (COLO678 and NCI-H716) and two breast cancer cell lines (EFM19 and MCF7) that are XRN1 resistant (Figure 2A). These cell lines were selected to represent a range of XRN1 sensitivity and a range of XRN1 resistance (Figure 2A). To further explore our findings in clinically relevant models, we also included the patient-derived colon cancer stem cell (CSC)-enriched spheroid line POP92.[25,26] To validate the results from our DepMap analysis, we knocked out XRN1 in these models with CRISPR-Cas9 (Figure S2B). The XRN1-sensitive cell lines NCI-H747 and C84 had highly reduced cell numbers 5 days after XRN1 knockout compared to the XRN1-resistant cell lines NCI-H716 and COLO678 (Figures 2B and S2C). Additionally, we validated that the XRN1-sensitive cell lines NCI-H747 and C84 had elevated expression of ISGs at baseline compared to the XRN1-resistant cell lines COLO678 and NCI-H716 (Figure 2C). POP92 cells have low ISG expression and are not sensitive to XRN1 knockout, categorizing them as XRN1 resistant (Figures 2B and 2C). Similarly, the XRN1-sensitive breast cancer cell lines HCC202 and MDA-MB-468 have lower viability upon XRN1 knockout and higher ISG expression at baseline compared to the XRN1-resistant breast cancer cell lines MCF7 and EFM19 (Figures 2D, 2E, and S2C).

To investigate whether dependency on XRN1 is related to its enzymatic function, we used CRISPR longitudinal assay profiling specific edits (LAPSE) in NCI-H747 cells. In brief, CRISPR-Cas9 is used to create mixed populations of cells, which are sequenced over time to quantify growth of wild-type and mutant cells. To validate this method, we introduced XRN1-targeting Cas9-ribonucleoproteins (RNPs) and observed reduced viability in XRN1-knockout (KO) populations relative to unedited, wild-type cells (Figure S2D). To evaluate the effect of an endogenous XRN1 catalytic mutation (D208A),[27,28] we introduced another XRN1-targeting Cas9-RNP along with one of two donor oligos for homology-directed repair (HDR). We not only observed that cells with a D208A catalytic mutation grew more slowly than those with a silent wild-type (WT) mutation (D208D) but also that D208A mutant cells grew similarly to XRN1-KO cells (Figures 2F and S2E). These results show that XRN1 catalytic activity is important for maintaining the viability of XRN1-sensitive cancer cells.

Next, we sought to determine if the level of XRN1 or other RNA decay proteins would explain which cell lines were dependent on XRN1. Neither XRN1 protein levels nor XRN1 expression significantly correlate to sensitivity to XRN1 loss (Figures S3A and S3B). XRN1 levels in most of the cell lines selected for experiments do not correlate with whether the cell line is XRN1 sensitive or not (Figures S3C and S3D). Overall, expression of genes associated with IFN response, but not genes associated with the GO term "RNA catabolic process," correlate with sensitivity to XRN1 loss (Figures S3E and S3F). The major exception is OAS2, which is an ISG (Figure S3E). Therefore, the level of RNA decay proteins does not explain the difference in XRN1 dependency. Instead, we sought to determine differences in baseline dsRNA levels between XRN1-sensitive and XRN1-resistant cell lines. Dot blots of total RNA using the J2 antibody, which recognizes dsRNA helixes longer than 40 bp, revealed elevated dsRNA levels in XRN1-sensitive cell lines compared to XRN1-resistant cell lines (Figure 3A). Confocal imaging staining for dsRNA with the J2 antibody confirmed the increased presence of cytosolic dsRNA in the XRN1-sensitive cell lines NCI-H747 and C84 compared to the XRN1-resistant cell lines COLO678 and NCI-H716 (Figure 3B).

To assess what could be the source of these elevated dsRNA levels, we acquired a table of sequences with calculated dsRNA force from Šulc et al.[29] These are the unique complementary sequences that are the most likely to form dsRNA for 3 kb windows of the genome. To assess which of these sequences with dsRNA force could contribute to the effect of XRN1 knockout on viability, we did a differential expression analysis to reveal which of the sequences with dsRNA force significantly correlated to the effect of XRN1 knockout on viability in the DepMap dataset (Figure 3C). To confirm that this analysis enriched for correlating sequences, we calculated the total sum per cell line of the sequences with dsRNA force that had a significant correlation with the effect of XRN1 knockout on the viability of cell lines (red square in Figure 3C) and found a significant linear correlation (Figure 3D). A subset of repeats can form IRs and are therefore a source of dsRNA in cells[5]; we therefore looked at the distribution of IRs in sequences with dsRNA force, revealing that most of them are not overlapping with IRs (Figure 3E). However, not all of the sequences with dsRNA force can form dsRNA, only those with a high dsRNA force are likely to do so. We therefore redid the linear correlation from Figure 3D with sequences with a dsRNA force higher than 0.5 (Figure 3F). We also highlight how the expression of one such dsRNA force region is expressed in selected cell lines on the regression line and those selected for experiments (Figures S3G–S3I). Interestingly, this analysis increased the linear correlation with the effect of XRN1 knockout on viability, and 87% of these high-dsRNA-force sequences overlap with IR-Alus (Figure 3G). In agreement with our previous observation that XRN1 protein levels did not correlate with XRN1 sensitivity, there is also no correlation between high-dsRNA-force regions predictive of XRN1 sensitivity and XRN1 protein level (Figure S3J). Collectively, XRN1 dependency is associated with elevated ISG expression and higher levels of cytosolic dsRNA and correlates with a subset of IR-Alus capable of forming dsRNA, which are all hallmarks of viral mimicry induction.

Pharmacological induction of cytosolic dsRNA produces a synthetic dependency on XRN1

We next sought to determine whether increased levels of cytosolic dsRNA could sensitize XRN1-resistant cells to XRN1 inhibition. DNA-demethylating agents such as 5-AZA-CdR and CDK4/6 inhibitors such as palbociclib can induce viral mimicry by increasing the level of cytosolic dsRNA.[3,4,30] Immunostaining in POP92 XRN1-knockout cells with the J2 antibody revealed a significant increase in cytoplasmic dsRNA in XRN1-depleted cells treated with 5-AZA-CdR compared to control cells (Figure 4A). XRN1 knockout led to a significant reduction of the 5-AZA-CdR half-maximal effective concentration (EC50) *in vitro* (Figures 4B and S4A). Furthermore, 5-AZA-CdR sensitized the XRN1-resistant colorectal cancer cell lines COLO678 and NCI-H716 as well as the XRN1-resistant breast cancer cell lines MCF7 and EFM19 to XRN1 knockout (Figure S4B). The EC50 of palbociclib was also reduced by over 5-fold in POP92 cells with XRN1 knocked out compared to controls (Figure 4C). Like 5-AZA-CdR, palbociclib induces a synthetic dependency on XRN1 in both XRN1-resistant breast and colon cancer cell lines (Figure S4C). Collectively, these results suggest that sensitivity to XRN1 may be mediated by cytoplasmic dsRNA levels and that XRN1-resistant cell lines can be sensitized to XRN1 knockout by increasing dsRNA levels with viral-mimicry-inducing drugs.

MAVS and PKR activation mediates sensitivity to XRN1 disruption

Cytosolic dsRNAs can trigger an innate immune response upon recognition by cytosolic RNA-sensing receptors such as MDA5 and PKR. Upon dsRNA recognition, MDA5 promotes aggregation of MAVS on the mitochondrial membrane and activates type I/III IFN signaling to induce the expression of ISGs. PKR and ribonuclease L (RNaseL) exert antiviral activity through translational arrest and RNA degradation, respectively.[31,32] To investigate the mechanism of cell lethality after depletion of XRN1, we knocked out MAVS, PKR, and RNaseL (Figure 5A). In the XRN1-sensitive cell line NCI-H747, we found that both MAVS knockout and PKR knockout partially rescued cell lethality after XRN1 knockout (Figures 5B, 5C, and S5A). Double knockout of MAVS and PKR was able to almost completely

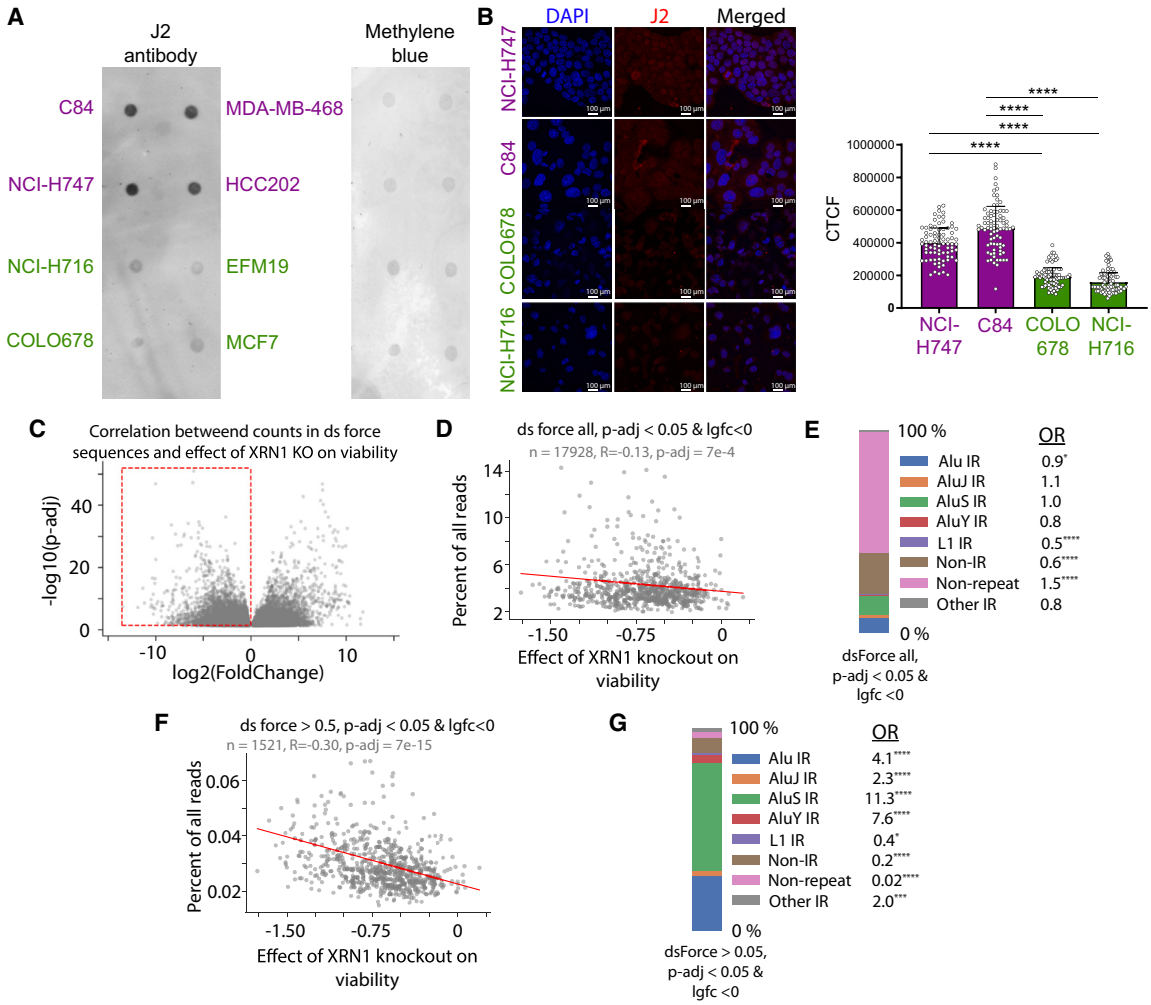

Figure 3. XRN1 dependency is associated with higher levels of dsRNA and higher levels of a subset of IR-Alus capable of forming dsRNA

(A) Dot blot for dsRNA using total RNA from indicated cell lines. Normalized amounts of total RNA were dotted on Hybond N+ membranes, visualized by methylene blue staining, and immunoblotted with J2 antibody.

(B) Representative confocal microscopy images of colorectal cell lines as well as quantification of images with each dot being a cell and error bars showing standard deviation. Nuclei were stained with DAPI (blue), and dsRNA was stained using the J2 antibody (red). Representative of two biological replicates. p values were calculated using Bonferroni two-way ANOVA.

(C) Volcano plot of which sequences with dsRNA force from Šulc et al.[29] correlate with effect of XRN1 knockout on viability in the DepMap dataset. Counts per sequence with dsRNA force were calculated for each cell line in the CCLE (n = 665), and DESeq2 was used to find the correlation between the effect of XRN1 knockout on viability and count. Each dot is one sequence with dsRNA force, and the red square highlights selected sequences with dsRNA force.

(D) Percentage of reads that overlap with sequences highlighted in red square in (C). Each dot is one cell line out of 665 cell lines, and n is significantly correlating sequences with dsRNA force out of 3,611,307 sequences.

(E) Each sequence with dsRNA force used in (C) has a seqA and the complementary seqB; if the largest overlap with seqA is Alus and seqB has the largest overlap to another AluS, then the sequence is annotated as an Alus IR. Alu IR is when seqA and seqB overlap with different Alu subgroups. Non-IRs have matches in repeats but were not IRs. Non-repeat did not align to repeats. Other IR is categorized as an IR but with low percentage. Odds ratio (OR) represents enrichment or depletion compared to annotation for all dsRNA force regions, and p values were determined with two-sided Fisher's exact test, *$p < 10^{-2}$, **$p < 10^{-3}$, ***$p < 10^{-4}$, and ****$p < 10^{-5}$.

(F) Sequences with dsRNA force from (D) with dsRNA force higher than 0.5, indicating a high likelihood to form dsRNA.

(G) Annotations of sequences with dsRNA force from (F); see (E) for further explanation.

rescue the loss of viability in NCI-H747 cells with knockout of XRN1, indicating that these are the major pathways involved in mediating the observed cell viability effects of XRN1 depletion. However, deletion of RNaseL could not rescue cell lethality, indicating that RNaseL is dispensable for this phenotype. Although both MAVS and PKR knockout can affect *ISG15* expression after XRN1 knockout in NCI-H747 cells, we find that MAVS knockout decreases *ISG15* expression to a higher degree than PKR knockout (Figure 5D). Loss of both PKR and MAVS abrogates XRN1-knockout-induced *ISG15* expression (Figure 5D). We

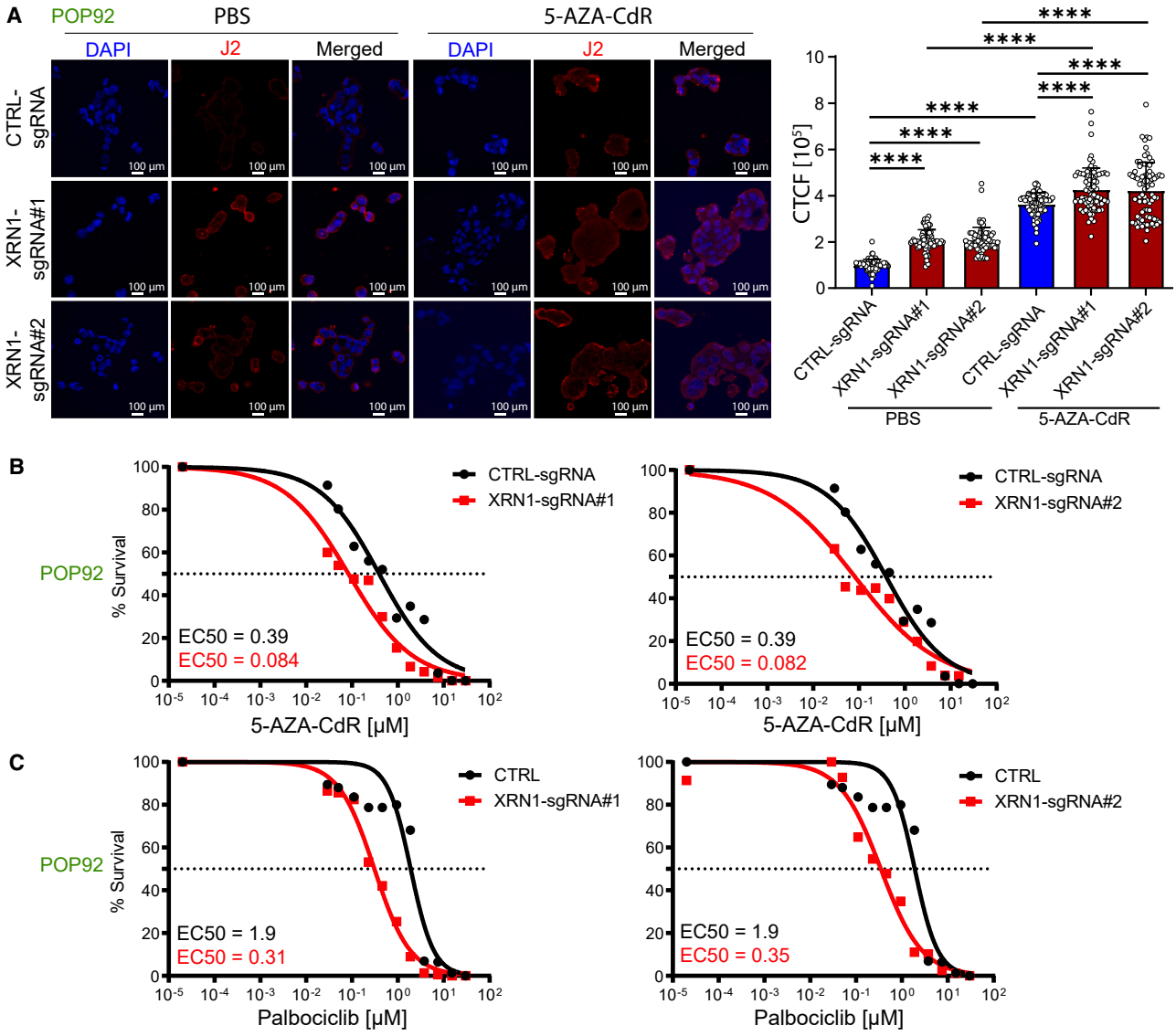

Figure 4. dsRNA induced by 5-AZA-CdR or palbociclib produces a synthetic dependency to XRN1 in XRN1-resistant POP92 cells

(A) Representative confocal microscopy images from control and knockout of XRN1 of POP92 cells treated with PBS or 5-AZA-CdR as well as quantification of images with each dot being a cell and error bars showing standard deviation. Nuclei were stained with DAPI (blue), and dsRNA was stained using the J2 antibody (red). Representative of two biological replicates. p values were calculated using Bonferroni two-way ANOVA.

(B) Survival of wild-type XRN1 (black) and XRN1-knockout (red) patient-derived CRC cells (POP92) after treatment with 5-AZA-CdR. The luminescence signal was normalized, and dose-response curves and EC50 values were calculated using a non-linear regression curve fit.

(C) Survival of wild-type XRN1 (black) and XRN1-knockout (red) POP92 cells after treatment with palbociclib. The luminescent signal was normalized, and dose-response curves and EC50 values were calculated using a non-linear regression curve fit.

also confirmed that NCI-H747 cells have elevated levels of IRF7 and ISG15 protein when XRN1 is knocked out (Figure S5B).

The induction of ISGs indicates that the IFN pathway could also play a role in cell lethality after XRN1 knockout. Supporting this, XRN1 knockout leads to higher IFN-β and IFN-λ expression in the XRN1-sensitive cell line NCI-H747 cells, and this expression is dependent on MAVS (Figure S5C). The addition of IFN-β could also block the partial rescue of XRN1 knockout provided by MAVS in NCI-H747 cells (Figure S5D). Additionally, the JAK1/2 inhibitor ruxolitinib[33] partly rescued sensitivity to XRN1 in NCI-H747 cells (Figures S5E and S5F). Together, these results show that IFN-β can play a role in MAVS-dependent cell death from loss of XRN1. However, other studies have reported both that IFN signaling is crucial for XRN1 and ADAR1 sensitivity and that it is not,[22,23,34] suggesting that whether IFN signaling is crucial for the sensitivity to these genes is system dependent.

Since 5-AZA-CdR leads to a synthetic XRN1 dependency in XRN1-resistant cells (Figures 4B and S4B), we investigated how the loss of MAVS, PKR, and RNaseL modulated the response to 5-AZA-CdR treatment in XRN1-knockout cells (Figure 5E,

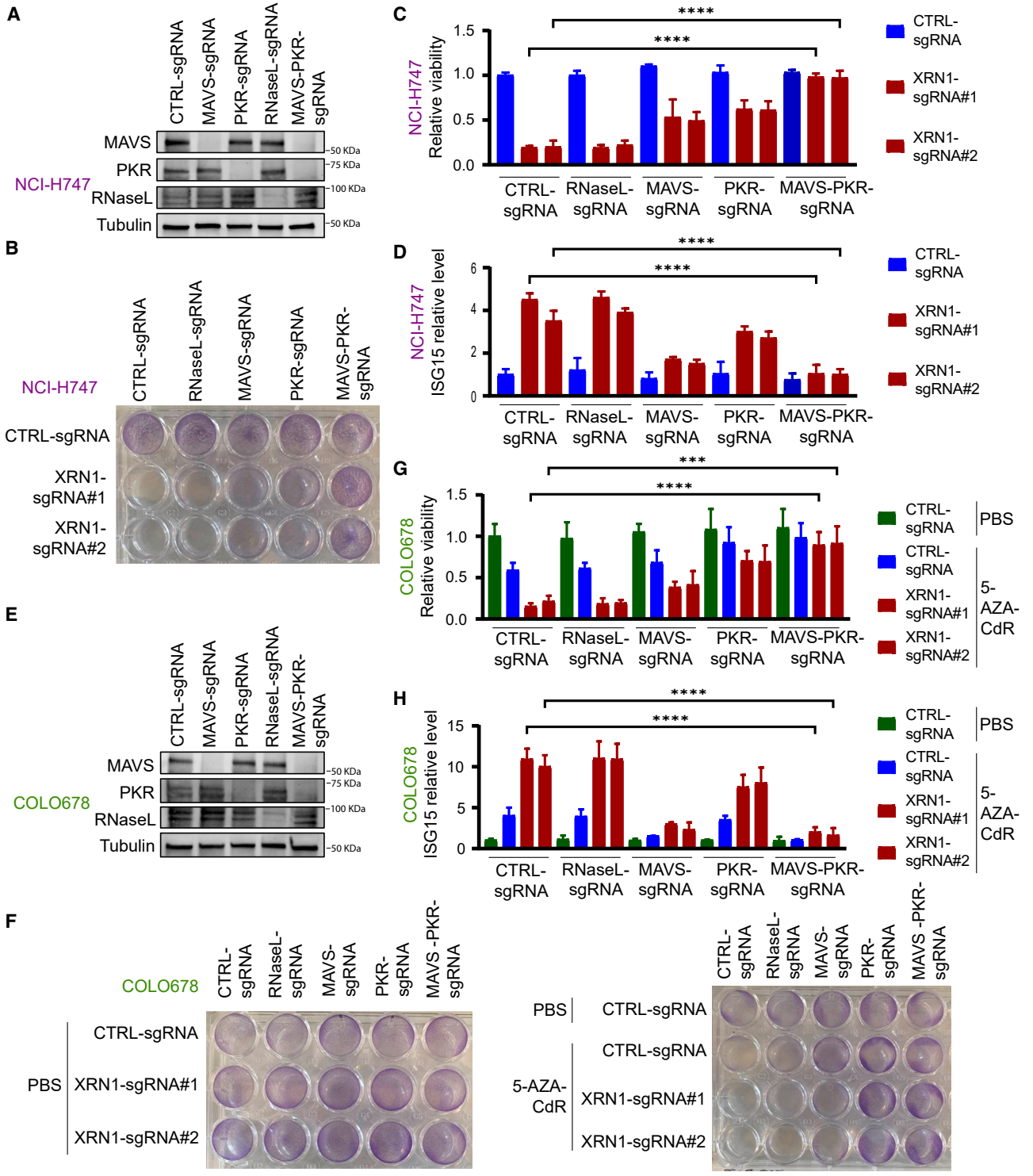

Figure 5. XRN1 dependency requires MAVS signaling and PKR activation

(A) Western blot of MAVS, PKR, and RNaseL protein levels in NCI-H747 cells. Tubulin is loading control.

(B) Cell viability in NCI-H747 cells by crystal violet staining.

(C) Cell viability in NCI-H747 cells by CellTiter-Glo assay. Data are presented as the mean of triplicates ±SD and p values were calculated using Bonferroni two-way ANOVA.

(D) qPCR of *ISG15* in NCI-H747 cells. Values are normalized against *RPLP0*. Data are presented as the mean of triplicates ±SD and p values were calculated using Bonferroni two-way ANOVA.

(legend continued on next page)

5F, and S5G). Similar to NCI-H747 cells, both MAVS and PKR knockout partly rescued the loss of viability upon XRN1 knockout in COLO678 cells treated with 5-AZA-CdR, but double knockout of MAVS and PKR completely rescued the loss in viability (Figures 5F and 5G). The degree of rescue observed with PKR knockout in COLO678 cells was more robust compared to cells with MAVS knockout, suggesting that PKR binding of the dsRNA induced by 5-AZA-CdR was mainly responsible for the observed cell death phenotype. On the contrary, MAVS knockout more strongly inhibited *ISG15* induction than PKR-knockout cells (Figure 5H). Altogether, these results suggest that while it is the MAVS pathway that is mainly responsible for ISG activation, both the MAVS and PKR pathways mediate XRN1-knockout-induced cell death. Furthermore, as both of these pathways induce cell death in response to dsRNA, these results highlight the importance of dsRNA in XRN1-dependent cell death.

XRN1 dependency is partly independent of ADAR1 activity

Cancer cells can avoid cell death induced by viral mimicry through ADAR1-dependent A-to-I editing, which shields dsRNAs from detection by innate immune receptors.[5,18] We therefore investigated whether ADAR1-dependent viral mimicry adaptation can inhibit XRN1-knockout-induced cell death. A-to-I editing levels in these cell lines were estimated by a modified pipeline based on variant calling in RNA sequencing (RNA-seq) data from the CCLE[19] and revealed active A-to-I editing with 19,255 and 20,023 A-to-I editing loci in the XRN1-resistant cell lines NCI-H716 and COLO678, respectively, and 24,808 A-to-I editing loci in the XRN1-sensitive cell line NCI-H747 (Figure 6A). Furthermore, between 30% and 43% of these A-to-I edits are found in Alus. To investigate the interaction between A-to-I editing and XRN1-knockout-induced viral mimicry, we generated POP92 ADAR1-knockdown cells (Figure S6A). Both POP92 cells with ADAR1 knockdown and XRN1 knockout have reduced viability upon treatment with 5-AZA-CdR; however, the reduction in viability was not enhanced by simultaneous XRN1 and ADAR1 depletion (Figure 6B). Interestingly, we found higher ISG expression when XRN1 was depleted in 5-AZA-CdR-treated cells (Figure 6C). Furthermore, we found that ADAR1 overexpression is associated with increased cell viability and lower ISG expression compared to controls after treatment with 5-AZA-CdR (Figures S6B and S6C), confirming that ADAR1 can function as a viral mimicry adaptation mechanism.[5]

Interestingly, XRN1 knockout in combination with 5-AZA-CdR in POP92 cells leads to a reduction in cellular viability despite ADAR1-dependent viral mimicry adaptation (Figure 6D). We found higher levels of ISG expression after combined depletion of XRN1 and ADAR1 relative to ADAR1 depletion alone, indicating that XRN1 and ADAR1 together regulate ISG expression from viral mimicry activation (Figure 6C). However, ADAR1 overexpression was able to prevent ISG induction in XRN1-knockout cells treated with 5-AZA-CdR (Figure 6E). Next, we measured aggregation of the mitochondrial protein MAVS in the mitochondria fraction of cell lysates. MAVS aggregation assays confirmed that MAVS aggregates upon treatment with 5-AZA-CdR and that ADAR1 overexpression was enough to prevent the MAVS aggregation in XRN1-knockout cell lines treated with 5-AZA-CdR (Figures 6F and 6G). These results suggest that ADAR1 can counteract the activation of the MDA5/MAVS pathway, but not PKR-induced cell death, upon XRN1 knockout. These results indicate that targeting XRN1 could have anti-cancer effects that are independent of viral mimicry adaptation by ADAR1 and highlight the therapeutic potential of XRN1.

DISCUSSION

To escape the mechanisms limiting cellular growth in normal cells, cancer cells must disrupt normal cellular processes. However, disruption to certain cellular mechanisms regulating expression and RNA metabolism can also lead to the presence of immunogenic endogenous retroelements and induce viral mimicry.[15] To avoid viral-mimicry-induced cell death, cancer cells are dependent on viral mimicry adaptation mechanisms such as A-to-I editing of dsRNA by ADAR1.[5] Here, we correlated ISG expression, a readout of the antiviral state in the cell, with the effect of gene knockout on viability to survey potential viral mimicry dependencies. Among the top hits, we found the RNA decay protein XRN1. Elevated levels of dsRNA and ISG expression were associated with the reduction in viability observed upon XRN1 knockout, which was rescued by double knockout of MAVS and PKR. These are all hallmarks of viral mimicry induction and confirm that the reduction in viability following XRN1 knockout occurs through induction of viral mimicry.

The most well-described source of endogenous stimuli that can activate viral mimicry are dsRNAs from IR-Alus.[5,18] It is therefore not surprising that proteins associated with RNA processing, such as XRN1, appeared among the viral mimicry adaptation mechanisms appearing in our screen. The most direct explanation for how disrupting XRN1 leads to an antiviral state in the cell is that dsRNA, which otherwise would have been degraded by XRN1, accumulates in the cytoplasm, where it can activate the innate immune receptors MDA5 and PKR. Furthermore, our work demonstrates that XRN1-sensitive cell lines already have elevated dsRNA levels as measured by the J2 antibody and thus may be closer to crossing a "threshold" of tolerable dsRNA levels that XRN1 depletion pushes them past. Additional evidence for this mechanism comes from the fact that XRN1-resistant cell lines that have low baseline dsRNA levels can be made sensitive through treatment with dsRNA-elevating drugs like 5-AZA-CdR or palbociclib, suggesting that XRN1 knockout alone is ineffective in these cells because it

(E) Western blot of MAVS, PKR, and RNaseL protein levels in COLO678 cells. Tubulin is loading control.
(F) Cell viability in COLO678 cells by crystal violet staining.
(G) Cell viability in COLO678 by CellTiter-Glo assay. Data are presented as the mean of triplicates ±SD and p values were calculated using Bonferroni two-way ANOVA.
(H) qPCR of *ISG15* in COLO678 cells. Values are normalized against *RPLP0*. Data are presented as the mean of triplicates ±SD and p values were calculated using Bonferroni two-way ANOVA.

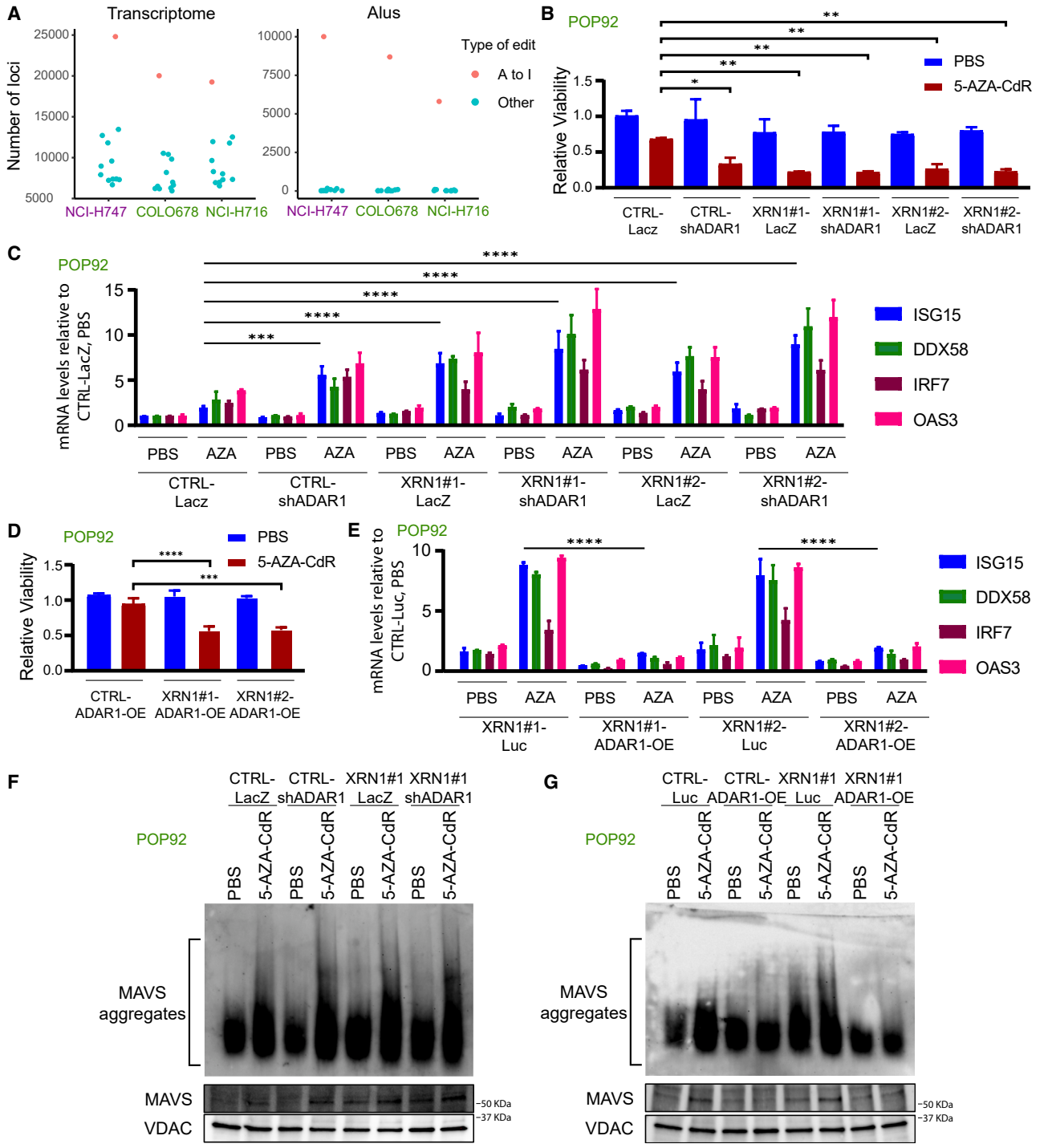

Figure 6. XRN1 depletion can kill cancer cells despite viral mimicry adaptation by high expression of ADAR1

(A) Number of A-to-I-edited loci in the transcriptome and only in Alus in indicated cell lines. Others represent other variants than A to I such as G to C, A to C, etc.

(B) Cell viability in POP92 cells with indicated knockout determined with CellTiter-Glo assay. Data are presented as the mean of triplicates ±SD and p values were calculated using Bonferroni two-way ANOVA.

(C) PCR of selected ISGs in POP92 cells with indicated knockout and overexpression of ADAR1 and XRN1. Values are normalized against RPLP0. Data are presented as the mean of triplicates ±SD and p values were calculated using Bonferroni two-way ANOVA. Significance levels are shown for ISG15 but are equal for the other genes.

(legend continued on next page)

cannot push their low baseline levels of dsRNA beyond a tolerable threshold. Finally, the complete rescue of loss in viability by XRN1 knockout when we knock out MAVS and PKR (Figures 5C and 5G) indicates that mechanisms upstream of MAVS and PKR are the main modulators of these pathways. This includes dsRNA sensing by MDA5 and PKR. However, we cannot rule out the role of molecules other than dsRNA in loss of cell viability upon loss of XRN1. Nevertheless, these results indicate that XRN1-dependent degradation of RNA is an important mechanism that prevents the accumulation of dsRNA beyond the threshold required for activation of viral mimicry.

We find that XRN1-knockout-induced cell death is mediated by both MAVS and PKR. We show that MAVS-dependent cell death upon knockout of XRN1 is associated with higher ISG induction, implicating activation of antiviral pathways in this phenotype. PKR-mediated cell death, on the other hand, appears to occur more directly without ISG induction. The fact that PKR and MDA5 are activated by dsRNA of different lengths supports the observation that these two pathways can act independently of each other. PKR can be activated from dsRNA that is as short as 30 bp, while MDA5 preferentially activates the IFN pathway through MAVS from longer dsRNA molecules.[35] Disagreeing results from investigations into ADAR1 dependency suggest that which pathway is responsible for cell death might be system dependent. Liu et al. found that both MAVS and PKR knockout can partly rescue ADAR1 dependency in a tongue cancer cell line,[23] while Gannon et al. found that only PKR knockout could partly rescue ADAR1 dependency in lung cancer cell lines.[22] Hu et al. found that ADAR1-mediated editing of dsRNA disrupts activation of MDA5, while dsRNA binding of ADAR1p150 disrupts activation of PKR, and that knock out of both PKR and MDA5 is needed to rescue embryonic lethality in *ADAR1p150*$^{-/-}$ mice, allowing them to live to adulthood.[36] It is also likely that the role of MDA5/MAVS and PKR is system dependent in XRN1 dependency. Two studies done in parallel to this work have found different roles for MAVS and PKR in XRN1 dependency. Ran et al. found that MAVS knockout abolished the tumor-suppressive effect of XRN1 silencing in a melanoma xenograft mouse model,[37] while Zou et al. could rescue XRN1 dependency in lung cancer cells by knocking out PKR but not MAVS.[34]

Additionally, our results indicate that XRN1 and ADAR1 dependencies have different effects on cell death pathways. We found that ADAR1 overexpression can inhibit XRN1-knockout-induced expression of ISGs; however, XRN1 knockout reduced cell numbers even when ADAR1 was overexpressed. Future studies should investigate the limit of ADAR1's ability to inhibit MDA5-MAVS induced cell death. However, it is possible that XRN1 is able to evade ADAR1-dependent resistance to viral-mimicry-induced cell death, which could make it an attractive drug target.

Induction of viral mimicry can be a mechanism for treating cancer either by enhancing cancer cell killing by immune cells or by leading to activation of internal cell death pathways in the cancer cell.[2] Ran et al. found that silencing XRN1 can potentiate immunotherapy efficiency in mice.[37] They found that disruption of XRN1 activated the IFN pathway through MAVS signaling. Knocking out *Pkr*, *Sting*, or *Mda5* in mice did not completely rescue the ISG induction seen in cells where XRN1 function is disrupted, indicating that XRN1 can induce viral mimicry through multiple pathways. Interestingly, this study did not find that XRN1 knockout itself inhibited the cell growth of the mouse tumor cells, indicating that the tumor model they used may be similar to the XRN1-resistant cell lines described here. Our work suggests that disrupting XRN1 alone in an XRN1-resistant tumor would be unlikely to clear the cancer. However, we were able to create a synthetic XRN1 dependency by treating cells with the viral-mimicry-inducing drugs 5-AZA-CdR and palbociclib. Alternatively, it would be interesting to see if XRN1 can be targeted in tumors with a high baseline induction of viral mimicry. For example, gliomas with the tumor-driving K27M mutation in histone 3 (H3K27M) redistribute H3K27 acetylation and have increased expression of endogenous retroelements, possibly introducing a vulnerability to XRN1 depletion.[38] Similarly, R882 is a hotspot for mutations in DNMT3A in acute myeloid leukemia, and this mutation can lead to expression of immunogenic endogenous retroelements.[39] Rhabdoid tumors could also be a potential target, as they are driven by biallelic inactivation of SMARCB1, which also leads to expression of endogenous retroelements.[40] Finally, XRN1 exhibits a multifaceted involvement across various cancer types, supported by evidence demonstrating its downregulation in osteosarcoma.[41,42] This implies that targeting XRN1 could hold therapeutic promise in specific cancer subtypes. However, additional research is needed to precisely delineate the specific cancer subtypes that could benefit from targeting XRN1.

In addition to inhibiting viral mimicry induction in cells, XRN1 has also been found to be important in the response to viral infections. In combination with viral decapping enzymes, XRN1 can facilitate the replication of the vaccinia virus by limiting ISG-inducing dsRNA accumulation.[43] Alternatively, it is possible that degradation of viral RNA can itself pose a threat to viral replication. This is supported by the finding that certain flaviviruses have developed a specific RNA secondary structure that can resist degradation by XRN1.[44] The role of XRN1 in the antiviral response is further highlighted by work by Ran et al. suggesting that XRN1 itself is an ISG whose expression can be induced by IFN-α or IFN-γ.[37] Together, these results highlight that XRN1 is an important regulator of the antiviral state in the cell, both in exogenous viral infection and endogenous viral mimicry activation.

Here, we evaluate viral mimicry dependencies across the genome and systematically identify targets regulating viral mimicry such as XRN1. XRN1-sensitive cell lines have a higher baseline level of dsRNA and ISGs, while XRN1-resistant cell lines can be made synthetically dependent on XRN1 through viral-mimicry-inducing drugs. These results underline the potential for targeting XRN1 in the development of cancer therapeutics against

(D) See (B).
(E) See (C).
(F and G) Western blot of MAVS showing aggregation after indicated treatment in POP92 cells with indicated knockout of XRN1 and knockdown or overexpression of ADAR1. VDAC is loading control.

cancers with a high baseline induction in viral mimicry or in combination with viral-mimicry-inducing drugs. Interestingly, XRN1 depletion even leads to cell death in cells with ADAR1 overexpression, which can otherwise inhibit viral-mimicry-dependent cell death, highlighting that XRN1 is a biologically distinct target. Further research is needed to determine exactly where and when XRN1 is important for degrading endogenous dsRNA and to establish biomarkers that indicate candidate tumors for XRN1-targeted cancer therapeutics. However, what is clear is that there is a close link between XRN1 and the antiviral state of the cell. Furthermore, these results validate our screening approach for the discovery of viral mimicry dependencies and suggest that the other hits identified here merit further validation as cancer therapeutic targets.

Limitations of the study

As the results here are based upon human cell lines, they cannot directly be applied to human cancer cells *in vivo*. Furthermore, the observation that only some cell lines are sensitive to XRN1 depletion makes it clear that future research is required to know which human cancer types are sensitive to XRN1 depletion, which cancer types can be made sensitive to XRN1 depletion with dsRNA-inducing drugs, and for which cancer types XRN1 cannot be targeted. Additionally, some of the results in Figures 1, 3, and S1 are based upon correlations that cannot be used to infer causation. Follow-up experiments confirm some of the observations in Figure 1, such as XRN1 being a viral mimicry dependency, but care should be taken when interpreting results solely based on correlations. Finally, XRN1 protein levels were not assessed after introducing the D208A mutation for catalytically dead XRN1 in the CRISPR LAPSE experiment due to difficulties presented by the dynamic mixed-population nature of the experiment. Therefore, we cannot definitively rule out that this mutation could have influenced XRN1 levels in our results. However, other reports have demonstrated that XRN1, in other models harboring D208A or similar mutations, expresses at similar levels to WT XRN1.[34,45,46]

STAR★METHODS

Detailed methods are provided in the online version of this paper and include the following:

- KEY RESOURCES TABLE
- RESOURCE AVAILABILITY
  - Lead contact
  - Materials availability
  - Data and code availability
- EXPERIMENTAL MODEL AND STUDY PARTICIPANT DETAILS
- METHOD DETAILS
  - Primary cell and Cell line growth conditions
  - CRISPR knockout
  - *In vitro* studies and viability assays
  - Crystal violet staining
  - Western blot analysis
  - Total RNA extraction and RT-qPCR
  - Dot blot
  - MAVS aggregation assay
  - Immunofluorescence confocal microscopy
  - Linear correlation analysis
  - Linear correlation to sequences with dsRNA force
  - STRING gene networks and enrichment analysis
  - Genome-wide search for RNA editing
  - CRISPR LAPSE
- QUANTIFICATION AND STATISTICAL ANALYSIS

SUPPLEMENTAL INFORMATION

Supplemental information can be found online at https://doi.org/10.1016/j.celrep.2024.113684.

ACKNOWLEDGMENTS

We thank Catherine O'Brien for providing the POP92 cells and Simona Cocco for the collaboration on dsRNA forces. D.D.D.C. reports grants from the Princess Margaret Cancer Foundation, the Canadian Institutes of Health Research, the Canada Research Chair, and from Pfizer. A.D.G. was supported by the European Union's Horizon 2020 research and innovation program under the Marie Sklodowska-Curie grant agreement no. 101026293.

AUTHOR CONTRIBUTIONS

A.H., H.T.L., R.C., and D.D.D.C. contributed to conceptualization and study design. A.H., R.C., P.M., P.C.M., and M.C. performed experiments with input from C.A.I. H.T.L. and S.A.M. performed bioinformatics data analysis. A.D.G. and B.G. gave input on the dsRNA force analysis. A.H., H.T.L., R.C., and D.D.D.C. wrote the original draft, with feedback from the other authors.

DECLARATION OF INTERESTS

D.D.D.C. is co-founder, holds shares in and serves in a leadership position at Adela, Inc. outside the submitted work. B.G. has received honoraria for speaking engagements from Merck, Bristol Meyers Squibb, and Chugai Pharmaceuticals; has received research funding from Bristol Meyers Squibb, Merck, and ROME Therapeutics; and has been a compensated consultant for Darwin Health, Merck, PMV Pharma, Shennon Biotechnologies, and Rome Therapeutics, of which he is a co-founder.

Received: July 6, 2023
Revised: October 31, 2023
Accepted: January 3, 2024

REFERENCES

1. Katze, M.G., He, Y., and Gale, M. (2002). Viruses and interferon: a fight for supremacy. Nat. Rev. Immunol. *2*, 675–687.
2. Chen, R., Ishak, C.A., and De Carvalho, D.D. (2021). Endogenous Retroelements and the Viral Mimicry Response in Cancer Therapy and Cellular Homeostasis. Cancer Discov. *11*, 2707–2725.
3. Roulois, D., Loo Yau, H., Singhania, R., Wang, Y., Danesh, A., Shen, S.Y., Han, H., Liang, G., Jones, P.A., Pugh, T.J., et al. (2015). DNA-Demethylating Agents Target Colorectal Cancer Cells by Inducing Viral Mimicry by Endogenous Transcripts. Cell *162*, 961–973.
4. Chiappinelli, K.B., Strissel, P.L., Desrichard, A., Li, H., Henke, C., Akman, B., Hein, A., Rote, N.S., Cope, L.M., Snyder, A., et al. (2015). Inhibiting DNA Methylation Causes an Interferon Response in Cancer via dsRNA Including Endogenous Retroviruses. Cell *162*, 974–986.
5. Mehdipour, P., Marhon, S.A., Ettayebi, I., Chakravarthy, A., Hosseini, A., Wang, Y., de Castro, F.A., Loo Yau, H., Ishak, C., Abelson, S., et al. (2020). Epigenetic therapy induces transcription of inverted SINEs and ADAR1 dependency. Nature *588*, 169–173.

6. Sheng, W., LaFleur, M.W., Nguyen, T.H., Chen, S., Chakravarthy, A., Conway, J.R., Li, Y., Chen, H., Yang, H., Hsu, P.-H., et al. (2018). LSD1 Ablation Stimulates Anti-tumor Immunity and Enables Checkpoint Blockade. Cell *174*, 549–563.e19.
7. Bowling, E.A., Wang, J.H., Gong, F., Wu, W., Neill, N.J., Kim, I.S., Tyagi, S., Orellana, M., Kurley, S.J., Dominguez-Vidaña, R., et al. (2021). Spliceosome-targeted therapies trigger an antiviral immune response in triple-negative breast cancer. Cell *184*, 384–403.e21.
8. Ishizuka, J.J., Manguso, R.T., Cheruiyot, C.K., Bi, K., Panda, A., Iracheta-Vellve, A., Miller, B.C., Du, P.P., Yates, K.B., Dubrot, J., et al. (2019). Loss of ADAR1 in tumours overcomes resistance to immune checkpoint blockade. Nature *565*, 43–48.
9. Wells, J.N., and Feschotte, C. (2020). A Field Guide to Eukaryotic Transposable Elements. Annu. Rev. Genet. *54*, 539–561.
10. Griffin, G.K., Wu, J., Iracheta-Vellve, A., Patti, J.C., Hsu, J., Davis, T., Dele-Oni, D., Du, P.P., Halawi, A.G., Ishizuka, J.J., et al. (2021). Epigenetic silencing by SETDB1 suppresses tumour intrinsic immunogenicity. Nature *595*, 309–314.
11. Wu, Q., Nie, D.Y., Ba-alawi, W., Ji, Y., Zhang, Z., Cruickshank, J., Haight, J., Ciamponi, F.E., Chen, J., Duan, S., et al. (2022). PRMT inhibition induces a viral mimicry response in triple-negative breast cancer. Nat. Chem. Biol. *18*, 821–830.
12. Chelmicki, T., Roger, E., Teissandier, A., Dura, M., Bonneville, L., Rucli, S., Dossin, F., Fouassier, C., Lameiras, S., and Bourc'his, D. (2021). m6A RNA methylation regulates the fate of endogenous retroviruses. Nature *591*, 312–316.
13. Qiu, W., Zhang, Q., Zhang, R., Lu, Y., Wang, X., Tian, H., Yang, Y., Gu, Z., Gao, Y., Yang, X., et al. (2021). N6-methyladenosine RNA modification suppresses antiviral innate sensing pathways via reshaping double-stranded RNA. Nat. Commun. *12*, 1582.
14. Gao, Y., Vasic, R., Song, Y., Teng, R., Liu, C., Gbyli, R., Biancon, G., Nelakanti, R., Lobben, K., Kudo, E., et al. (2020). m6A Modification Prevents Formation of Endogenous Double-Stranded RNAs and Deleterious Innate Immune Responses during Hematopoietic Development. Immunity *52*, 1007–1021.e8.
15. Lindholm, H.T., Chen, R., and De Carvalho, D.D. (2023). Endogenous retroelements as alarms for disruptions to cellular homeostasis. Trends Cancer *9*, 55–68.
16. Eisenberg, E., and Levanon, E.Y. (2018). A-to-I RNA editing — immune protector and transcriptome diversifier. Nat. Rev. Genet. *19*, 473–490.
17. Lander, E.S., Linton, L.M., Birren, B., Nusbaum, C., Zody, M.C., Baldwin, J., Devon, K., Dewar, K., Doyle, M., FitzHugh, W., et al. (2001). Initial sequencing and analysis of the human genome. Nature *409*, 860–921.
18. Ahmad, S., Mu, X., Yang, F., Greenwald, E., Park, J.W., Jacob, E., Zhang, C.-Z., and Hur, S. (2018). Breaching Self-Tolerance to Alu Duplex RNA Underlies MDA5-Mediated Inflammation. Cell *172*, 797–810.e13.
19. Ghandi, M., Huang, F.W., Jané-Valbuena, J., Kryukov, G.V., Lo, C.C., McDonald, E.R., Barretina, J., Gelfand, E.T., Bielski, C.M., Li, H., et al. (2019). Next-generation characterization of the Cancer Cell Line Encyclopedia. Nature *569*, 503–508.
20. Dempster, J.M., Boyle, I., Vazquez, F., Root, D.E., Boehm, J.S., Hahn, W.C., Tsherniak, A., and McFarland, J.M. (2021). Chronos: a cell population dynamics model of CRISPR experiments that improves inference of gene fitness effects. Genome Biol. *22*, 343.
21. Jones, C.I., Zabolotskaya, M.V., and Newbury, S.F. (2012). The 5′ → 3′ exoribonuclease XRN1/Pacman and its functions in cellular processes and development. WIREs RNA *3*, 455–468.
22. Gannon, H.S., Zou, T., Kiessling, M.K., Gao, G.F., Cai, D., Choi, P.S., Ivan, A.P., Buchumenski, I., Berger, A.C., Goldstein, J.T., et al. (2018). Identification of ADAR1 adenosine deaminase dependency in a subset of cancer cells. Nat. Commun. *9*, 5450.
23. Liu, H., Golji, J., Brodeur, L.K., Chung, F.S., Chen, J.T., deBeaumont, R.S., Bullock, C.P., Jones, M.D., Kerr, G., Li, L., et al. (2019). Tumor-derived IFN triggers chronic pathway agonism and sensitivity to ADAR loss. Nat. Med. *25*, 95–102.
24. Szklarczyk, D., Gable, A.L., Lyon, D., Junge, A., Wyder, S., Huerta-Cepas, J., Simonovic, M., Doncheva, N.T., Morris, J.H., Bork, P., et al. (2019). STRING v11: protein-protein association networks with increased coverage, supporting functional discovery in genome-wide experimental datasets. Nucleic Acids Res. *47*, D607–D613.
25. O'Brien, C.A., Kreso, A., Ryan, P., Hermans, K.G., Gibson, L., Wang, Y., Tsatsanis, A., Gallinger, S., and Dick, J.E. (2012). ID1 and ID3 Regulate the Self-Renewal Capacity of Human Colon Cancer-Initiating Cells through p21. Cancer Cell *21*, 777–792.
26. Gao, S., Soares, F., Wang, S., Wong, C.C., Chen, H., Yang, Z., Liu, W., Go, M.Y.Y., Ahmed, M., Zeng, Y., et al. (2021). CRISPR screens identify cholesterol biosynthesis as a therapeutic target on stemness and drug resistance of colon cancer. Oncogene *40*, 6601–6613.
27. Jinek, M., Coyle, S.M., and Doudna, J.A. (2011). Coupled 5′ Nucleotide Recognition and Processivity in Xrn1-Mediated mRNA Decay. Mol. Cell *41*, 600–608.
28. Solinger, J.A., Pascolini, D., and Heyer, W.-D. (1999). Active-Site Mutations in the Xrn1p Exoribonuclease of Saccharomyces cerevisiae Reveal a Specific Role in Meiosis. Mol. Cell Biol. *19*, 5930–5942.
29. Šulc, P., Gioacchino, A.D., Solovyov, A., Marhon, S.A., Sun, S., Lindholm, H.T., Chen, R., Hosseini, A., Jiang, H., Ly, B.-H., et al. (2023). Repeats Mimic Pathogen-Associated Patterns across a Vast Evolutionary Landscape. Preprint at bioRxiv. https://www.biorxiv.org/content/10.1101/2021.11.04.467016v2.
30. Goel, S., DeCristo, M.J., Watt, A.C., BrinJones, H., Sceneay, J., Li, B.B., Khan, N., Ubellacker, J.M., Xie, S., Metzger-Filho, O., et al. (2017). CDK4/6 inhibition triggers anti-tumor immunity. Nature *548*, 471–475.
31. Gal-Ben-Ari, S., Barrera, I., Ehrlich, M., and Rosenblum, K. (2018). PKR: A Kinase to Remember. Front. Mol. Neurosci. *11*, 480.
32. Li, Y., Banerjee, S., Goldstein, S.A., Dong, B., Gaughan, C., Rath, S., Donovan, J., Korennykh, A., Silverman, R.H., and Weiss, S.R. (2017). Ribonuclease L mediates the cell-lethal phenotype of double-stranded RNA editing enzyme ADAR1 deficiency in a human cell line. Elife *6*, e25687.
33. Mesa, R.A., Yasothan, U., and Kirkpatrick, P. (2012). Nat. Rev. Drug Discov. *11*, 103–104.
34. Zou, T., Zhou, M., Gupta, A., Zhuang, P., Fishbein, A.R., Wei, H.Y., Zhang, Z., Cherniack, A.D., and Meyerson, M. (2023). XRN1 deletion induces PKR-dependent cell lethality in interferon-activated cancer cells. Cell Reports *43*, 113600.
35. Chen, Y.G., and Hur, S. (2021). Cellular origins of dsRNA, their recognition and consequences. Nat. Rev. Mol. Cell Biol. *23*, 286–301.
36. Hu, S.-B., Heraud-Farlow, J., Sun, T., Liang, Z., Goradia, A., Taylor, S., Walkley, C.R., and Li, J.B. (2023). ADAR1p150 Prevents MDA5 and PKR Activation via Distinct Mechanisms to Avert Fatal Autoinflammation.
37. Ran, X.-B., Ding, L.-W., Sun, Q.-Y., Yang, H., Said, J.W., Zhentang, L., Madan, V., Dakle, P., Xiao, J.-F., Loh, X., et al. (2023). Targeting RNA Exonuclease XRN1 Potentiates Efficacy of Cancer Immunotherapy (Cancer Res.). CAN-21-3052.
38. Krug, B., De Jay, N., Harutyunyan, A.S., Deshmukh, S., Marchione, D.M., Guilhamon, P., Bertrand, K.C., Mikael, L.G., McConechy, M.K., Chen, C.C.L., et al. (2019). Pervasive H3K27 Acetylation Leads to ERV Expression and a Therapeutic Vulnerability in H3K27M Gliomas. Cancer Cell *35*, 782–797.e8.
39. Scheller, M., Ludwig, A.K., Göllner, S., Rohde, C., Krämer, S., Stäble, S., Janssen, M., Müller, J.A., He, L., Bäumer, N., et al. (2021). Hotspot DNMT3A mutations in clonal hematopoiesis and acute myeloid leukemia sensitize cells to azacytidine via viral mimicry response. Nat. Cancer *2*, 527–544.
40. Leruste, A., Tosello, J., Ramos, R.N., Tauziède-Espariat, A., Brohard, S., Han, Z.-Y., Beccaria, K., Andrianteranagna, M., Caudana, P., Nikolic, J., et al. (2019). Clonally Expanded T Cells Reveal Immunogenicity of Rhabdoid Tumors. Cancer Cell *36*, 597–612.e8.

41. Pashler, A.L., Towler, B.P., Jones, C.I., Haime, H.J., Burgess, T., and Newbury, S.F. (2021). Genome-wide analyses of XRN1-sensitive targets in osteosarcoma cells identify disease-relevant transcripts containing G-rich motifs. RNA *27*, 1265–1280.

42. Pashler, A.L., Towler, B.P., Jones, C.I., and Newbury, S.F. (2016). The roles of the exoribonucleases DIS3L2 and XRN1 in human disease. Biochem. Soc. Trans. *44*, 1377–1384.

43. Burgess, H.M., and Mohr, I. (2015). Cellular 5′-3′ mRNA Exonuclease Xrn1 Controls Double-Stranded RNA Accumulation and Anti-Viral Responses. Cell Host Microbe *17*, 332–344.

44. Chapman, E.G., Costantino, D.A., Rabe, J.L., Moon, S.L., Wilusz, J., Nix, J.C., and Kieft, J.S. (2014). The Structural Basis of Pathogenic Subgenomic Flavivirus RNA (sfRNA) Production. Science *344*, 307–310.

45. McGinnis, M.M., Sutter, B.M., Jahangiri, S., and Tu, B.P. (2023). Exonuclease Xrn1 regulates TORC1 signaling in response to SAM availability. Elife *12*.

46. Blasco-Moreno, B., de Campos-Mata, L., Böttcher, R., García-Martínez, J., Jungfleisch, J., Nedialkova, D.D., Chattopadhyay, S., Gas, M.-E., Oliva, B., Pérez-Ortín, J.E., et al. (2019). The exonuclease Xrn1 activates transcription and translation of mRNAs encoding membrane proteins. Nat. Commun. *10*, 1298.

47. Ettayebi, I., Yau, H.L., and De Carvalho, D.D. (2019). Methods to detect endogenous dsRNA induction and recognition. In Methods in Enzymology (Elsevier), pp. 35–51.

48. Dobin, A., Davis, C.A., Schlesinger, F., Drenkow, J., Zaleski, C., Jha, S., Batut, P., Chaisson, M., and Gingeras, T.R. (2013). STAR: ultrafast universal RNA-seq aligner. Bioinformatics *29*, 15–21.

49. Pertea, M., Pertea, G.M., Antonescu, C.M., Chang, T.-C., Mendell, J.T., and Salzberg, S.L. (2015). StringTie enables improved reconstruction of a transcriptome from RNA-seq reads. Nat. Biotechnol. *33*, 290–295.

50. Jun, G., Wing, M.K., Abecasis, G.R., and Kang, H.M. (2015). An efficient and scalable analysis framework for variant extraction and refinement from population-scale DNA sequence data. Genome Res. *25*, 918–925.

51. Narasimhan, V., Danecek, P., Scally, A., Xue, Y., Tyler-Smith, C., and Durbin, R. (2016). BCFtools/RoH: a hidden Markov model approach for detecting autozygosity from next-generation sequencing data. Bioinformatics *32*, 1749–1751.

52. Pinello, L., Canver, M.C., Hoban, M.D., Orkin, S.H., Kohn, D.B., Bauer, D.E., and Yuan, G.-C. (2016). Analyzing CRISPR genome-editing experiments with CRISPResso. Nat. Biotechnol. *34*, 695–697.

STAR★METHODS

KEY RESOURCES TABLE

REAGENT or RESOURCE	SOURCE	IDENTIFIER
Antibodies		
J2	SCICONS	Cat# 10010500; RRID:AB_2651015
MAVS	Abcam	Cat# ab89825; RRID:AB_2042274
RNaseL	Santa Cruz	Cat# sc-74405; RRID:AB_2181661
ADAR	Santa Cruz	Cat# sc-73408; RRID:AB_2222767
XRN1	Bethyl	Cat# A300-443A; RRID:AB_2219047
PKR	Cell Signaling	Cat# 3072; RRID:AB_2277600
ISG15	Santa Cruz	Cat# sc-166755; RRID:AB_2126308
IRF7	Cell Signaling	Cat# 13014S; RRID:AB_2737060
VDAC	Cell Signaling	Cat# 4661; RRID:AB_10557420
Alpha-tubulin	Sigma	Cat# T9026; RRID:AB_477593
Beta-actin	ThermoFisher	Cat# AM4302; RRID:AB_2536382
Vinculin	Cell Signaling	Cat# 13901S; RRID:AB_2728768
Anti-rabbit IgG,HRP-linked	Cell Signaling	Cat# 7074S; RRID:AB_2099233
Anti-mouseIgG,HRP-linked	Cell Signaling	Cat# 7076S; RRID:AB_330924
Anti-mouse IgG (H + L), $F(ab')_2$ Fragment (Alexa Fluor® 647 Conjugate)	Cell Signaling	Cat# 4410S; RRID:AB_1904023
Anti-rabbit IgG (H + L), $F(ab')_2$ Fragment (Alexa Fluor® 488 Conjugate)	Cell Signaling	Cat# 4412S; RRID:AB_1904025
Bacterial and virus strains		
pLBC2-BS-RFCA	John E.Dick lab	N/A
pLKO1	John E.Dick lab	N/A
Biological samples		
POP92	Princess Margaret Cancer Center	N/A
Chemicals, peptides, and recombinant proteins		
5-AZA-CdR	Sigma Aldrich	A3656
Palbociclib isethionate	Med Chem Express	HY-A0065
Insulin, Human Recombinant	Sigma-Aldrich	91077C
EGF Recombinant Human Protein	Thermofisher Scientific	PHG0313
Ruxolitinib	InvivoGen	tlrl-rux
Recombinant Human IFN-beta Protein	R&D Systems	8499-IF
Critical commercial assays		
RNeasy Mini Kit	Qiagen	74106
SuperScript Vilo IV	Thermo Fisher Scientific	11756050
Qproteome Mitochondria Isolation Kit	Qiagen	37612
Alt-R CRISPR-Cas9 System	Integrated DNA Technologies	N/A
Deposited data		
Cancer Cell Line Encyclopedia	European Nucleotide Archive	ENA: SRP186687
Experimental models: Cell lines		
NCI-H747	Cedarlane	CCL-252
C84	Sigma-Aldrich	12022902
COLO678	DSMZ	ACC 194
NCI-H716	Cedarlane	CCL-251
HCC202	Cedarlane	CRL-2316
MDA-MB-468	Cedarlane	HTB-132

(*Continued on next page*)

Continued

REAGENT or RESOURCE	SOURCE	IDENTIFIER
MCF7	Cedarlane	HTB-22
EFM19	DSMZ	ACC 231
Oligonucleotides		
RPLPO primer (CAGACAGACACTGGCAACA; ACATCTCCCCCTTCTCCTT)	IDT	N/A
ISG15 primer (GCCTCAGCTCTGACACC; CGAACTCATCTTTGCCAGTACA)	IDT	N/A
IRF7 primer (GTGGACTGAGGGCTTGTAG; TCAACACCTGTGACTTCATGT)	IDT	N/A
DDX58 primer (CCAGCATTACTAGTCAGAAGGAA; CACAGTGCAATCTTGTCATCC)	IDT	N/A
OAS2 primer (TTCTGCCTGCACCACTCTTCAACGA; GCCAGTCTTCAGAGCTGTGCCTTTG)	IDT	N/A
OAS3 primer (CCGAACTGTCCTGGGCCTGATCC; CCCATTCCCCAGGTCCCATGTGG)	IDT	N/A
IFN-b primers (Fwd-GCCATCAGTCACTTAAACAGC; Rev-GAAACTGAAGATCTCCTAGCCT)	IDT	N/A
IFN-l primers (Fwd-GAAGACAGGAGAGCTGCAAC; Rev-GGTTCAAATCTCTGTCACCACA)	IDT	N/A
CRISPR LAPSE primer - HPRT1 (ACACTCTTTCCCTACA CGACGCTCTTCCGATCTGCTCCCCTTCAATGGACACA; GACTGGAGTTCAGACGTGTGCTCTTCCGATCTATCCA ACACTTCGTGGGGTC)	IDT	N/A
CRISPR LAPSE primer - XRN1 sgRNA #3 (ACACTCTTTCCCTACACGACGCTCTTCCGATCTTGG GTGGAACAGATTTCTGTGAT; GACTGGAGTTCAGACGTG TGCTCTTCCGATCTACCATCTTCTCCAAAACCAGACT)	IDT	N/A
CRISPR LAPSE primer - XRN1 sgRNA #4 (ACACTCTTTCCC TACACGACGCTCTTCCGATCTAGTGAAAAGGCAACCTACGGA; GACTGGAGTTCAGACGTGTGCTCTTCCGATCT GGGGACAGGGGATAGGGTAA)	IDT	N/A
CRISPR LAPSE primer - XRN1 sgRNA #5, D208 HDR (ACACTCTTTCCCTACACGACGCTCTTCCGATCTTCA TGGCAAGGAGTTACCATCT; GACTGGAGTTCAGACGTG TGCTCTTCCGATCTTCTCCAATATTTGTTGCCACAGC)	IDT	N/A
CRISPR LAPSE - HPRT1 sgRNA (AATTATGGGGATTACTAGGA)	IDT	N/A
CRISPR LAPSE - XRN1 sgRNA #3 (ATATTACATGACGAAGATGG)	IDT	N/A
CRISPR LAPSE - XRN1 sgRNA #4 (GCTTGGATTAACAAGTCATG)	IDT	N/A
CRISPR LAPSE - XRN1 sgRNA #5 (D208 HDR) (GGTTTAGATGCTGACTTGGT)	IDT	N/A
CRISPR LAPSE HDR donor sequence. D208A + PAM mutant. ATCAATGCATAAGTTTATAATAATAAAAATTATAGCTACCAAG GCAGCATCTAAACCATAAAGACAGTGTCTGGTGTTTGGATC	IDT	N/A
CRISPR LAPSE HDR donor sequence. D208D + PAM mutant. ATCAATGCATAAGTTTATAATAATAAAAATTATAGCTACCAAA TCAGCATCTAAACCATAAAGACAGTGTCTGGTGTTTGGAT	IDT	N/A
pLKO.1 shADAR1:5′-CCGGGCCCACTGTTATCTTCACT TTCTCGAGAAAGTGAAGATAACAGTGGGCTTTTTG-3′	John E.Dick Lab	N/A
pLKO.1 LacZ:5′-CCGGTGTTGGCTTACGGCGGTGATTT CTCGAGAAATCACCGCCGTAAGCCAACTTTTTG-3′	John E.Dick Lab	N/A
XRN1-sgRNA#1, Hs.Cas9.XRN1.1.AA: 5′-TAATGCGAAACAACACCTCC-3′	IDT	N/A
XRN1-sgRNA#2, Hs.Cas9.XRN1.1.AB: 5′-GGAGTTACCATCTACTTCTC-3′	IDT	N/A

(*Continued on next page*)

Continued

REAGENT or RESOURCE	SOURCE	IDENTIFIER
Hs.Cas9.EIF2AK2.1.AA: 5′-TGGTACAGGTTCTACTAAAC-3′	IDT	N/A
Hs.Cas9.RNASEL.1.AA: 5′-CATCACTATCGTCAGAGCTC-3′	IDT	N/A
Hs.Cas9.MAVS.1.AC: 5′-GTAGATACAACTGACCCTGT-3′	IDT	N/A
Software and algorithms		
Python	Python Software Foundation	www.python.org
R	R Core Team	www.r-project.org
STAR	Alexander Dobin	github.com/alexdobin/STAR
Snakemake	Johannes Köster	snakemake.readthedocs.io
featureCounts	Subread	subread.sourceforge.net/
STRING	STRING Consortium 2023	string-db.org
Other		
CellTiter-Glo® Luminescent Cell Viability Assay	Promega	G7572
P3 PRIMARY CELL 4D-NUCLEOFECTOR KIT XS	Lonza	V4XP3032
Crystal Violet	Sigma-Aldrich	C0775
Sodium Pyruvate	Thermo Fisher Scientific	11360070
N2 supplement A	Stemcell Technologies	7152
Neurocult SM1	Stemcell Technologies	5711
Heparin	Sigma-Aldrich	H3149
Lipid Mixture 1	Sigma-Aldrich	L0288
HyClone™ Non Essential Amino Acids NEAA	Fisher Scientific	SH3023801

RESOURCE AVAILABILITY

Lead contact

Further information and requests for resources and reagents should be directed to and will be fulfilled by the lead contact, Daniel D. De Carvalho (daniel.decarvalho@uhnresearch.ca).

Materials availability

This study did not generate new unique reagents.

Data and code availability

(1) All data reported in this paper will be shared by the lead contact upon request.
(2) Code has been deposited to Zenodo: https://doi.org/10.5281/zenodo.10040059
(3) Any additional information required to reanalyze the data reported in this work paper is available from the lead contact upon request.

EXPERIMENTAL MODEL AND STUDY PARTICIPANT DETAILS

This study utilizes the following human cell lines models: NCI-H747 (male, 69, Cecum adenocarcinoma), C84 (male, 67, Cecum adenocarcinoma), COLO678 (male, 69, colon carcinoma), NCI-H716 (male, 33, Cecum adenocarcinoma), POP92 (primary colon tumor specimen), HCC202 (female, 82, Breast ductal carcinoma), MDA-MB-468 (female, 51, Breast adenocarcinoma), MCF7 (female, 69, Invasive breast carcinoma of no special type) and EFM19 (female, 50, Breast ductal carcinoma). See method details for maintenance and care conditions. Both cell lines from females and males are included in the study, although some experiments are only done in colon cancer cell lines which are from males.

METHOD DETAILS

Primary cell and Cell line growth conditions

NCI-H747, NCI-H716, COLO678, HCC202 and EFM19 cells were grown in RPMI-1640 medium with 10% (FBS) fetal bovine serum, 2mM glutamine and 1% penicillin/streptomycin. C84 cells were grown in IMDM medium with 10% FBS, 2mM glutamine and 1% Penicillin/Streptomycin. MCF7 cells were grown in DMEM medium with 10% FBS, 1 mM sodium pyruvate, 10 μg/mL human insulin,

0.1mM Non-Essential Amino Acids and 1% penicillin/streptomycin. Patient derived colorectal cells (POP92) were cultured in DMEM/F-12 supplemented with 1% penicillin/streptomycin, 0.1 mM Non-Essential amino acids, 1 mM sodium pyruvate, N2 supplement, NeuroCult SM1 Neuronal Supplement, 4 μg/mL heparin, 0.2% lipid mixture, 20 ng/mL EGF and 10 ng/mL basic FGF and 1% Penicillin/Streptomycin. NCI-H747 cells used in the CRISPR LAPSE experiment were grown in RPMI-1640 + GlutaMax (ThermoFisher 61870036) medium with 10% (FBS) fetal bovine serum (Corning 35-072-CV), 2.25 g/L D-glucose (Sigma G7021) and 1x penicillin/streptomycin (Gibco 15140-122). All cells were grown according to ATCC recommendations in a humidified tissue culture incubator at 37°C with 5% CO_2.

CRISPR knockout

CRISPR was performed using the Alt-R CRISPR-Cas9 System (Integrated DNA Technologies) as per manufacturer's protocol. Briefly, the ribonucleoprotein (RNP) complex was assembled by mixing of Alt-R CRISPR-Cas9 CrRNA with Alt-R CRISPR-Cas9 tracrRNA and Alt-R HiFi S.p. Cas9 Nuclease V3. Then cells were transfected with RNP complex by electroporation using pulse code EH115 and Lonza P3 primary cell 4D- Nucleofactor X Kit S (Basel, Switzerland).

In vitro studies and viability assays

The DNA methyltransferase inhibitor 5-AZA-CdR (A3656) was purchased from Sigma Aldrich. Palbociclib isethionate (HY-A0065) was purchased from Med Chem Express. For *in vitro* experiments, cells were treated with 5-AZA-CdR (300 nM), palbociclib (250 nM) and vehicle (PBS or DMSO) as treatment. Cells were kept in culture for 5 and 7 days for treatment with 5-AZA-CdR and palbociclib respectively. For interferon blockade and exogenous interferon treatment experiments, cells were treated with either ruxolitinib (Invivogen tlrl-rux, 1 μM) or IFN-β (R&D 8499-IF, 10 ng/mL) for 5 days. Cell viability was determined using a CellTiter-Glo luminescent cell viability assay (Promega). Data were presented as proliferation present by comparing the treated groups with the vehicle-treated cells.

Crystal violet staining

Cells were plated in 6-well tissue culture plates for 5 days. Each well was washed twice with ice-cold PBS on ice and fixed with 100% ice-cold methanol for about 10 min on ice. Then cells were stained with 0.5% crystal violet solution in 25% methanol for 10 min at room temperature, and the crystal violet stain removed by washing in water until the dye comes off. Fiji was used to quantify crystal violet staining. Circles were drawn to outline each well and the color threshold function was used to threshold the wells. The mean gray value for the thresholded image was measured and normalized to top well in each column before plotting.

Western blot analysis

Protein extracts were obtained from cell pellets after lysis with 100 μL–200 μL of sodium-dodecyl-sulfate (SDS) lysis buffer (2% SDS, 10% glycerol, 50 mM of Tris HCL) plus protease inhibitor cocktail (Sigma Aldrich, Catalog. No. 11836170001). Cell lysates were centrifuged for 15 min at 4°C, 13000 RPM. 20–40 μg of proteins were mixed with Laemmli (b-mercaptoethanol and bromophenol blue) and denatured for 10 min at 95°C. Cell lysates were loaded onto each lane of SDS-PAGE. Gel-separated proteins were transferred to a nitrocellulose membrane (Whatman) in a 1X transfer buffer containing 20% methanol, at 100V for 1 h at 4°C. Membranes were blocked with a solution of in TRIS-buffered saline (TBS: 20mM TRIS/HCl, pH 7.4, 137 mM NaCl, 2.7 mM KCl) plus 0.1% Tween (TBS-T) containing 5% non-fat dried milk. The same milk/TBS-T solution was prepared to dilute primary antibodies, which were incubated for 1 h at room temperature or overnight at 4°C. The next day, after 3 washes with 1% TBS-T (each wash 10 min), the membrane was incubated with the secondary HRP antibodies, diluted in 5% milk, for 30–60 min at room temperature. The membrane was washed again with TBS-T three times and ECL was applied for membrane development.

Total RNA extraction and RT-qPCR

For total RNA extraction, 1 mL TRIZOL reagent was added to cell pellets harvested from confluent cells. Cells were gently pipetted up and down for complete cell lysing in TRIZOL. TRIZOL/cell mixture was next transferred into a clean microcentrifuge tube and total RNA was purified using RNeasy Mini Kit (QIAGEN, Valencia, CA) and quantified by spectrophotometer (NanoDrop). Reverse transcription of 1 μg of RNA/sample was performed using SuperScript Vilo IV (Thermo Fisher Scientific) as per manufacturer's protocol.

5 to 10 ng of cDNA were used to perform quantitative polymerase chain reaction using 1X SsoAdvanced Universal SYBR Green Supermix (Bio-Rad). All RT-qPCR reactions were performed in a CFX Connect Real-Time PCR Detection System (Bio-Rad). Gene expression values were calculated by the ΔΔCq method, using *RPLP0* as the housekeeping gene, and resulting experimental target values were normalized to the global mean of the control group.

Dot blot

Purified RNA was dotted on Hybond N+ membrane (Amerhsam Hybond-N+), dried and autocross linked in a UV stratalinker 2400 (Stratagene) two times. The membrane was then blocked in 5% milk in PBS-T (0.1% Tween 20) for 30 min. Blocking buffer was discarded, and the membrane was incubated with J2 antibody rocking overnight at 4°C. Membrane was washed three times in PBS-T for 10 min at room temperature per wash. Membrane was then incubated with secondary goat-*anti*-mouse HRP antibody (Millipore cat#AP124P) in 5% milk at room temperature for 1 h. Washed membrane with PBS-T was subjected to chemiluminescent development. Membrane was stained with 0.5% methylene blue in 30% EtOH to visualize the presence of RNA.

MAVS aggregation assay

Semi-denaturing detergent agarose gel electrophoresis (SDD-AGE) was performed as previously described.[47] Briefly, mitochondria were isolated (Qproteome Mitochondria Isolation Kit, Qiagen) from from patient-derived CRC cells (POP92), resuspended in mitochondria buffer and diluted before loading on an a 1.5% agarose vertical gel at 4 °C at a constant voltage of 100 V in running buffer (1x TBE and 0.1% SDS) for 1 h. Proteins were then transferred into a nitrocellulose membrane, and MAVS protein was detected using anti-MAVS antibody (ab89825, Abcam)

Immunofluorescence confocal microscopy

Cells were fixed using cold methanol for 15 min at −20°C, washed three times with PBS and incubated with saturation buffer (PBS with 1% BSA) for 1 h. Cells were stained with primary antibody (anti-dsRNA clone J2, Scicons 10010500) and incubated overnight at 4°C. The next day, cells were washed three times for 10 min with PBS and incubated with secondary antibody (anti-mouse IgG (H + L), F(ab')2 Fragment (Alexa Fluor 647 Conjugate (Cell Signaling Technology, 4410) for 1 h at room temperature, and washed again three times for 10 min with PBS, and incubated with hoechst nuclear stain for 5 min. Cells were washed three times with PBS and mounted on a slide with ProLong Gold Antifade Mountant (Thermo Fisher Scientific, P36930). Confocal analysis was performed with a Zeiss LSM70 confocal microscope using a 40× oil immersion objective and images were then analyzed using ImageJ software. The corrected total cell fluorescence (CTCF) was determined by: integrated density − (area of selected cell × mean fluorescence of background readings). Cells from multiple fields of view of the same microscopy slide and at least two biological replicates were quantified.

Linear correlation analysis

CRISPR gene effect and CCLE expression for every gene was downloaded from the DepMap data downloads 22Q2.[20] Only cell lines with both effect and expression were included (n = 1005 cell lines). ISG score was determined by taking the mean of the *Z* score of the log2(TPM+1) values from the CCLE expression file for the 38 ISGs defined by Liu et al.,[23] see below for gene list. For every gene, the linear correlation between the ISG score and gene effect was calculated using the stats.linregress function from the python package scipy. The same approach was used for the other linear correlations in this manuscript.

38 ISGs from Liu et al.: ADAR, DDX60, HERC6, IRF7, OASL, PSME2, STAT2, TRIM25, BST2, DHX58, IFI35, ISG15, OGFR, RSAD2, TDRD7, UBE2L6, CASP1, EIF2AK2, IFIH1, ISG20, PARP12, RTP4, TRAFD1, USP18, CMPK2, EPSTI1, IFIT2, MX1, PARP14, SAMD9L, TRIM14, CXCL10, GBP4, IFIT3, NMI, PNPT1, SP110, TRIM21.

Linear correlation to sequences with dsRNA force

Fastq files from RNAseq for CCLE cell lines with the accession number ENA: SRP186687 were downloaded from the European Nucleotide Archive and aligned to the genome using STAR. Only cell lines that could be matched to cell line names used in DepMap were used (n = 665). The compressed version of a table describing the sequences most likely to form dsRNA across 3 kilobase windows of the genome with calculated dsRNA force was acquired from Šulc et al.[29] Every sequence has a seqA and a complementary seqB and featureCounts with the settings "-p -O -M -F" was used to count up reads for seqA and seqB individually. The counts for seqA and seqB were then added together for each sequence. The R package DESeq2 was used to find sequences with dsRNA force that had a statistical significant correlation with the effect of XRN1 knockout on viability in the DepMap dataset. For every cell line, the total amount of reads that aligned to significantly down-regulated sequences with dsRNA force was counted up and plotted in a scatterplot against the effect of XRN1 knockout on viability. Additionally, the total amount of reads that aligned to significantly down-regulated sequences with dsRNA force higher than 0.5 was counted up and plotted in a scatterplot against the effect of XRN1 knockout on viability. The stats.linregress function in the python package Scipy was used to calculate statistics for the linear regression, and the python package seaborn was used for plotting. Furthermore, sequences were overlapped with repeatmasker and it was assessed whether they were inverted repeats as described in Šulc et al.[29] For example, if the longest overlap for seqA was an AluY in the first strand and the longest overlap for seqB was an AluY in the second strand, the sequence was annotated as an AluY IR. Odds-ratios and corresponding p values were calculated using the fisher_exact function from the python package scipy.

STRING gene networks and enrichment analysis

Genelists were submitted to the STRING tool v11.5. Textmining, Experiments, Databases, co-expression, neighborhood, gene fusion and co-occurrence were all used as active interaction sources and medium confidence was used for interaction score. STRING was also used to perform enrichment analysis on the same gene list. The enrichment for the gene ontology "biological process" was downloaded. The 20 terms with the highest strength parameter from STRING were selected and plotted with the ggplot2 package in R.

Genome-wide search for RNA editing

The STAR aligner was used to align raw reads to the hg38 human genome,[48] allowing 10 mismatches per aligned read. Duplicate reads were marked and removed, and only unique reads were kept. To avoid bias due to library size, all bam files were down-sampled to 26 million reads. Transcripts were called from each sample using Stringtie,[49] and the called transcripts from all samples were

merged using the Stringtie merge mode. To prevent redundant coverage in read positions, the overlap between read mates was clipped using bamUtil clipoverlap,[50] and three base pairs at the start and end of reads were clipped using bamUtil trimbam due to potential errors. Reads aligned to insertions and deletions were discarded. Variants for each sample in merged transcript regions were called using the bcftools mpileup command,[51] with a minimum read position quality cutoff of Q = 20. Indel calling was ignored. Since the RNAseq samples are unstranded, we predicted the strandness of the loci based on several factors such as the strandness of the expressed genes that overlap with the genomic loci.

Filtering process was performed to remove mismatch positions that correspond to common SNPs in the SNP142 common database, which was downloaded from the UCSC genome browser table. A mismatch position is considered present if it has a read depth of at least 5 and if the read depth of the alternative nucleotide is at least 5% of the position read depth and a minimum of 2 reads; otherwise, it is considered absent. To assess editing at Alu elements, edited genomic loci were intersected with the whole genome Alu elements, and only edited loci that overlapped with Alus were kept, while other loci were filtered out.

CRISPR LAPSE

For knock-in/homology-directed repair (HDR), the RNP complex was supplemented with custom single-stranded DNA donor oligos (Integrated DNA Technologies) and cells were transfected by electroporation using setting #14 and the Neon Transfection System 100 μL Kit (Invitrogen, MPK10025). Media was supplemented with Alt-R HDR enhancer V2 (Integrated DNA Technologies, 10007921) for 24 h following electroporation to improve HDR.

Electroporation of cells with a unique Cas9-RNP/HDR donor combination results in a heterogeneous population with distinct genotypes: unedited/WT, indel, and knock-in (KI). For each unique sample (RNP/HDR donor combination), 5e5-1e6 cells were harvested 3- and 10-day post Cas9-RNP electroporation and genomic DNA was extracted for sequencing using the DNeasy Blood and Tissue Kit (Qiagen, 69506). PCR primers flanking CRISPR/Cas9 editing sites were designed to incorporate partial Illumina adapters compatible with Amplicon-EZ next generation sequencing service (Azenta). Amplicons were generated using the OneTaq PCR system (New England Biolabs, M0482L), purified using the Monarch PCR & DNA Cleanup Kit (T1030S), and submitted to Azenta for NGS. Raw FASTQ files were processed using CRISPResso version 1[52] to calculate the percentage of unedited/wild type (WT), frameshift/knockout (KO) and HDR/knock-in (KI) populations in each unique sample. To determine relative growth rates, each unique population was first normalized to its matched WT population (unique RNP/HDR donor and time point) before comparing between 10- and 3-day time points.

QUANTIFICATION AND STATISTICAL ANALYSIS

The number of replicates is stated in the figure legends. Unless otherwise stated, statistical analyses were performed using GraphPad prism (v7.0) using Bonferroni two-way ANOVA and statistical significance was determined at a p value <0.05. Unless otherwise mentioned asterisks indicate significance at these levels: * = $p \leq 0.05$, ** = $p \leq 0.01$, ***, $p \leq 0.001$, **** = $p \leq 0.0001$.

Cell Reports, Volume *43*

Supplemental information

Retroelement decay by the exonuclease XRN1 is a viral mimicry dependency in cancer

Amir Hosseini, Håvard T. Lindholm, Raymond Chen, Parinaz Mehdipour, Sajid A. Marhon, Charles A. Ishak, Paul C. Moore, Marie Classon, Andrea Di Gioacchino, Benjamin Greenbaum, and Daniel D. De Carvalho

Supplementary file

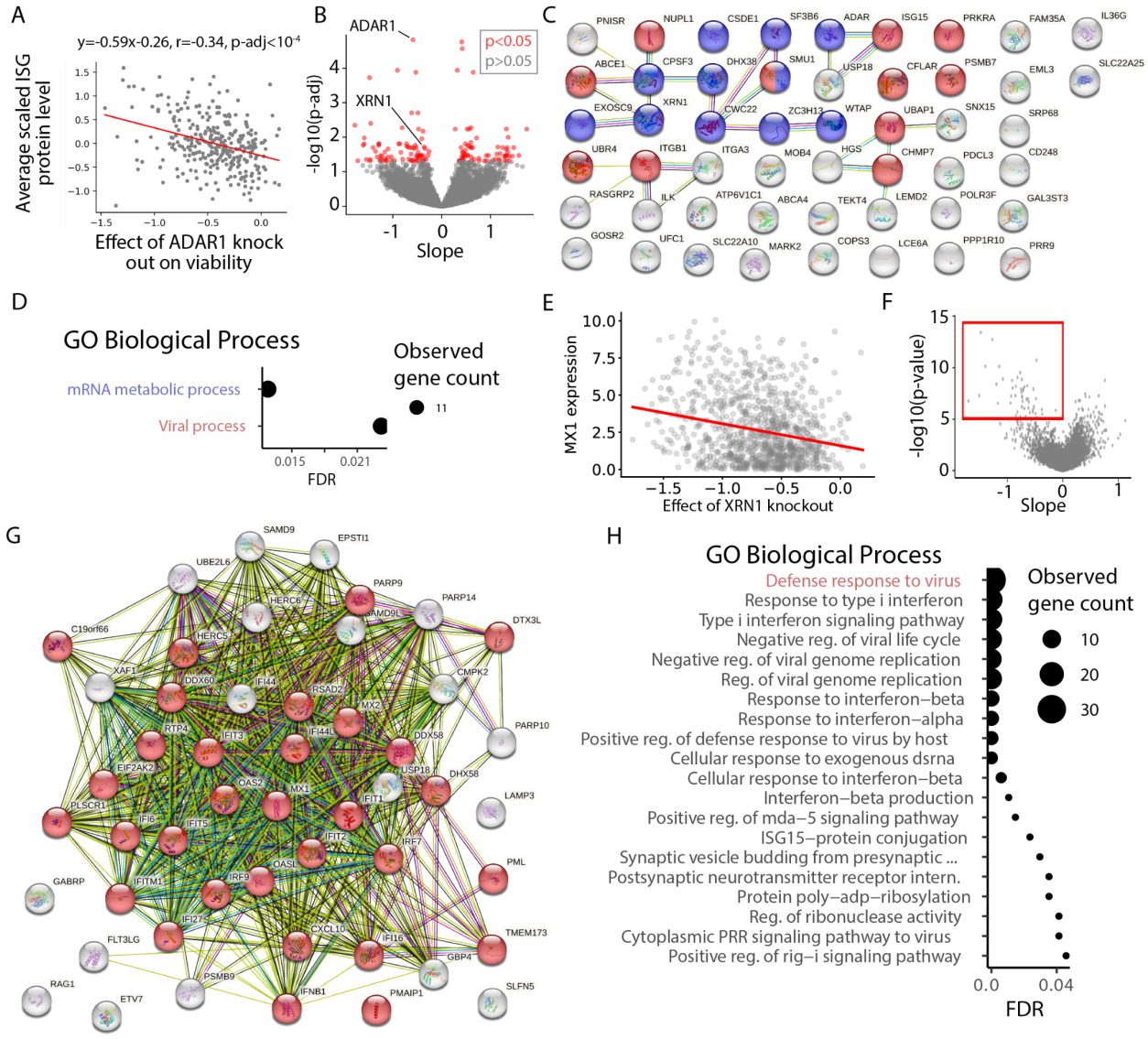

Figure S1. Correlation between effect of XRN1 knock out on viability and ISG expression. (A) Linear correlation of average scaled ISG protein levels of CCLE cell lines and effect on viability by knockout of XRN1 from the CRISPR DepMap dataset. Each dot is one cell line, and data from 302 cell lines[1]. The ISGs are 38 ISGs defined in Liu et al[2]. (B) Slope and adjusted p-value from linear correlation as done in A, shown for all genes. (C) Network of the 50 genes with the lowest p-value in the correlation of effect on viability from ADAR knockout and effect on viability from knocking out that gene. Made with the STRING tool. (D) All terms with FDR < 0.05 of the biological process GO terms according to the STRING tool. (E) Example of linear correlation analysis between gene expression from CCLE and effect on viability by knockout of XRN1 from the CRISPR DepMap dataset from 1005 cell lines. Here shown for the gene MX1. (F) Slope and p-value from linear correlation analysis as done in E. Red box shows the 50 genes with the lowest p-value with negative slope. (G) Network of the 50 genes with the lowest p-value in the correlation of effect on viability from XRN1 knockout and expression of that gene. Made with the STRING tool. (H) The 20 terms with the highest strength of the biological process GO terms according to the STRING tool. The color of GO term names corresponds to the node color seen in G.

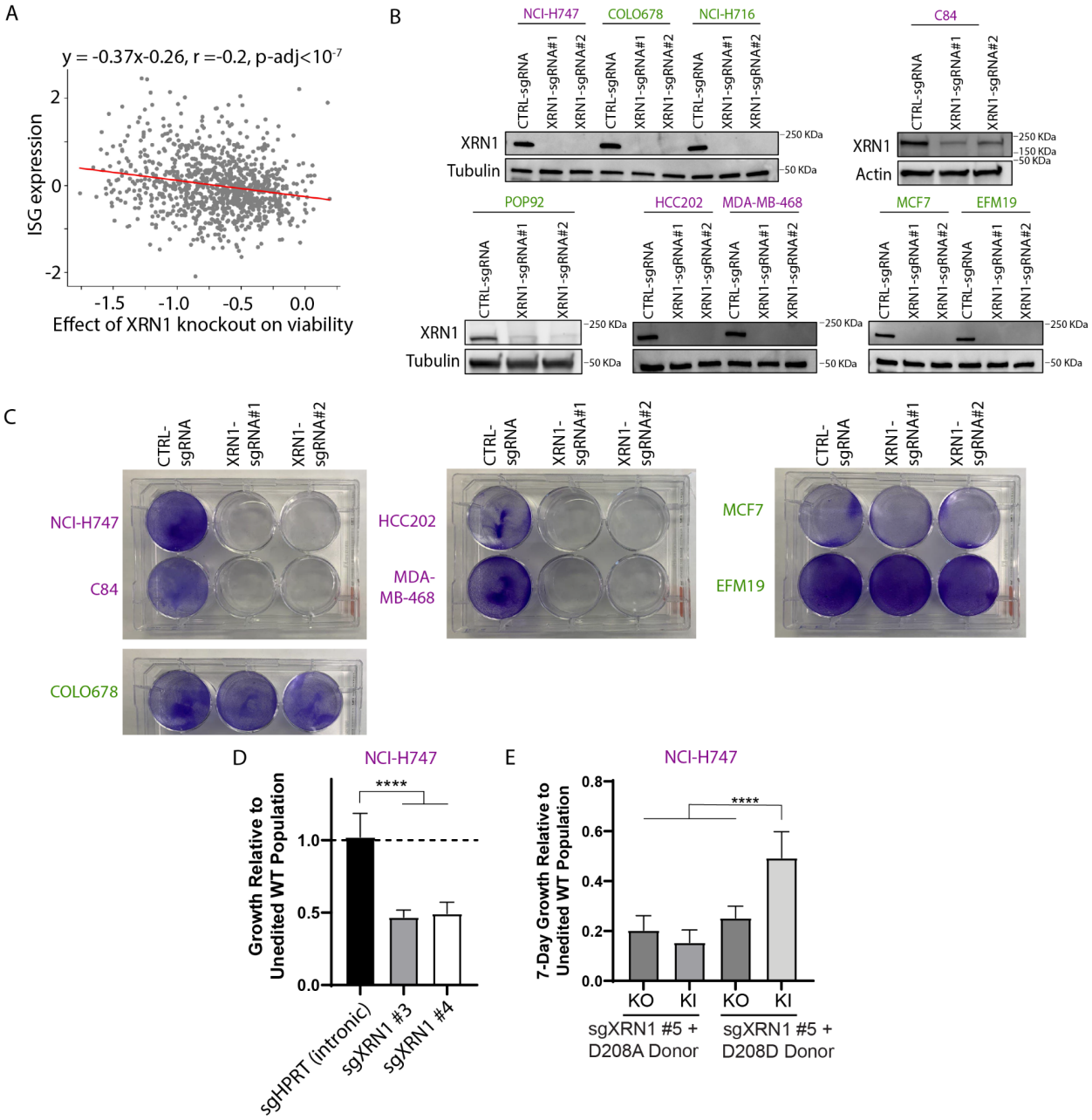

Figure S2. Viability of cell lines after XRN1 knockout. (A) Linear correlation between mean scaled ISG expression in the CCLE dataset of 38 ISGs defined by Liu et al[2] and effect on viability after knocking out XRN1 from the DepMap dataset. Each dot is a cell line. (B) Western blot of XRN1 protein level in indicated cell lines. XRN1-sensitive cell lines are colored purple and XRN1-resistant cell lines are colored green. Two independent clones were used for XRN1-KO. Tubulin or actin was used as a loading control. (C) Cell viability of control or XRN1-KO cells assessed by crystal violet staining. (D) CRISPR LAPSE in NCI-H747 using the indicated single-guide RNAs (sgRNA). 7-day fold change of the indicated frameshift (KO) subpopulations after normalizing to matched unedited (WT) subpopulations. Data presented as the mean of six experiments (five for sgHPRT1 sample) ± SD and p-values calculated with mixed-effects model (REML) with matched samples and assuming sphericity. (E) As in D, but with the inclusion of the indicated HDR donor oligos and concurrent analysis of distinct KO and knock-in (KI) subpopulations within each sample. Data presented as the mean of six experiments ± SD and p-values calculated with 1-way ANOVA with matched samples and assuming sphericity.

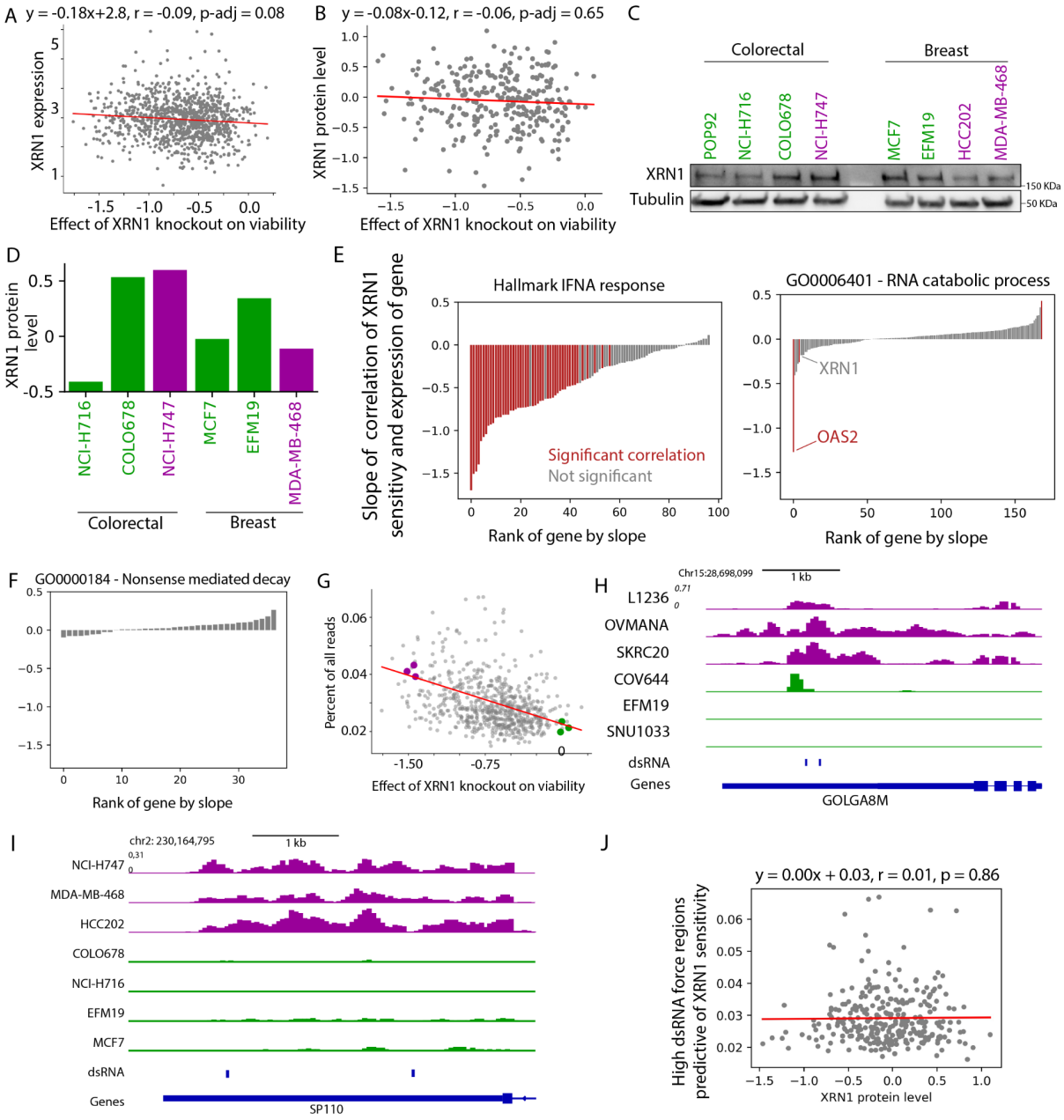

Figure S3. Correlating levels of RNA decay proteins to sensitivity to XRN1 knockout. (A) Linear correlation of XRN1 expression in the CCLE dataset and effect on viability after knocking out XRN1 from the DepMap dataset. Each dot is a cell line, n = 1005 cell lines. (B) Same as A except using quantitative proteomics data from cell lines[1]. n = 302 cell lines. (C) Western blot of XRN1 protein level in indicated cell lines. (D) Same quantitative proteomics data presented in B for cell lines used here that were available in the proteomic dataset. (E,F) The slope of linear correlation of XRN1 sensitivity and expression of a gene of all genes in the geneset indicated by the text above plot. GO genesets downloaded from AMIGO 2 and Hallmark geneset is from this paper[3]. Red bars indicate significantly correlating genes (p-adj < 0.05). G) Plot from figure 3F that highlights cell lines selected for displaying in H. H) Genomic signal from poly A based RNAseq from CCLE in selected cell lines. The dsRNA track represents one of the regions forming dsRNA that contribute to the score in G. As the y-axis in figure G shows the sum of 1521 fragments the value on the y-axis is not directly relatable to value on y-axis in H. I) Same as H but for a different region and showing the cell lines used here. J) Correlation between XRN1 protein level and high dsRNA force regions correlating with XRN1 sensitivity, see y-axis in figure 3F.

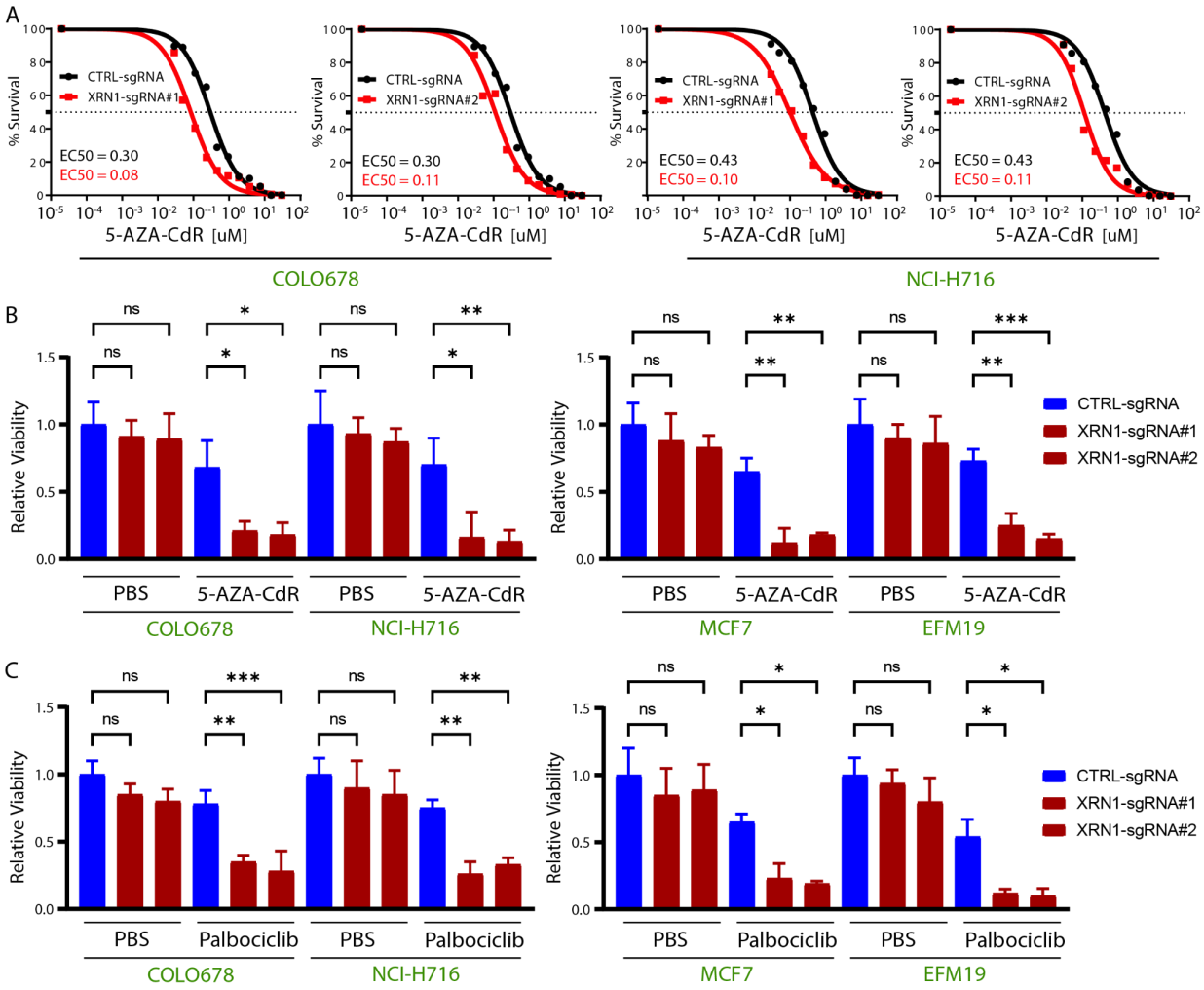

Figure S4. AZA and Palbociclib sensitizes XRN1-resistant cell lines to XRN1 knockout. (A) Survival of wild-type XRN1 (black) and XRN1-knockout (red) in indicated cells after treatment with 5-AZA-CdR. The luminescent signal was normalized, and dose-response curves and EC50 values were calculated using a nonlinear regression curve fit. (B) Cell viability was assessed by celltiter glo in CTRL and XRN1 KO Colorectal and breast cancer cells treated with 300 nM 5-AZA-CdR. (C) Cell viability was assessed by celltiter glo in CTRL and XRN1 KO Colorectal and breast cancer cells treated with Palbociclib. Data presented as the mean of triplicates ± SD.

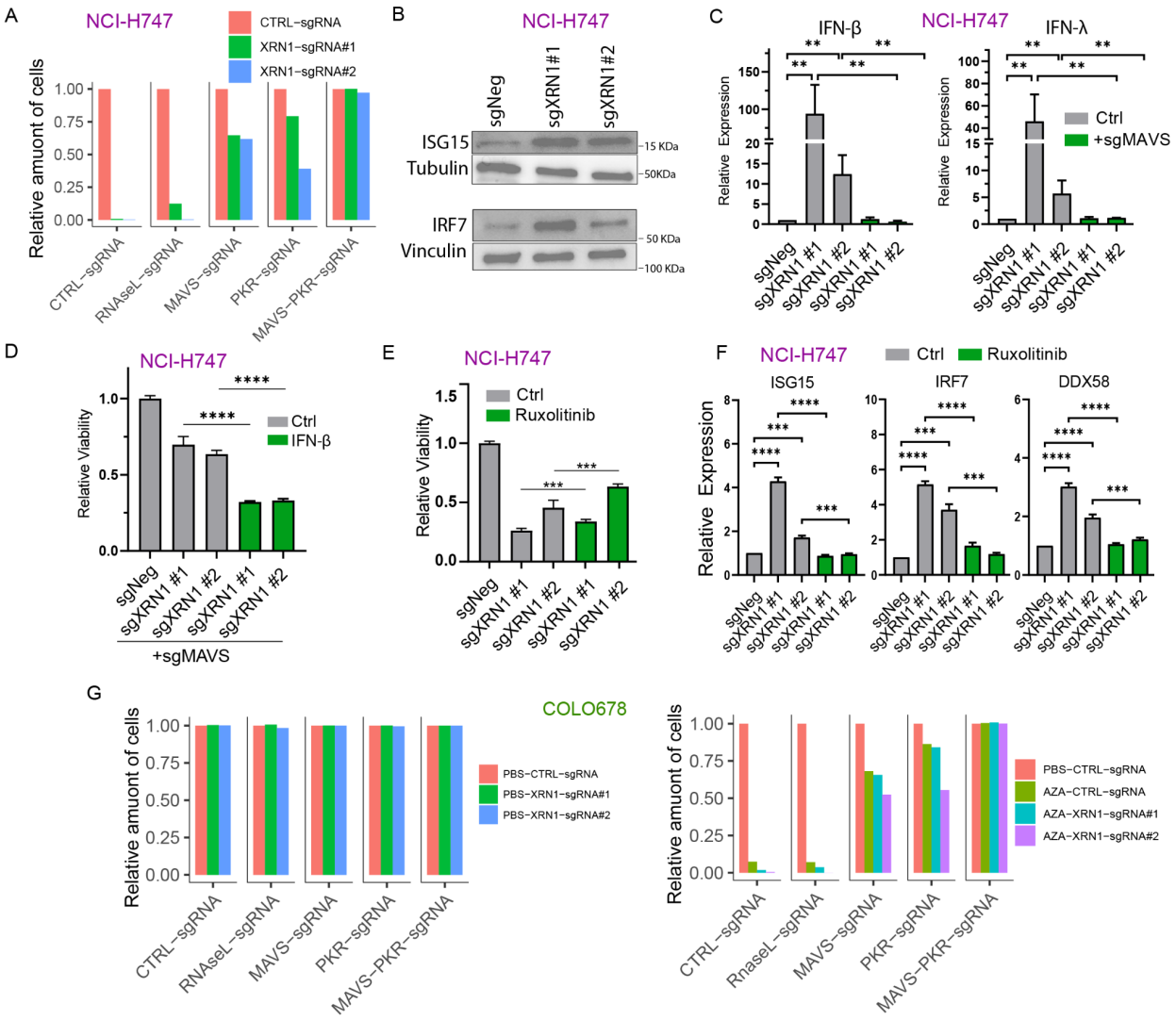

Figure S5. The role of the IFN pathway in XRN1 dependent cell death. A) Quantification of plate shown in 5B. B) Western blot after XRN1 knockout in NCI-H747 cells. C) qPCR of IFN genes in NCI-H747 cells with indicated knockout of MAVS. Values are normalized against RPLP0. Data presented as the mean of at least four technical replicates ± SD. D) Cell viability in MAVS knockout NCI-H747 cells assessed by celltiter glo in CTRL and XRN1 KO cells treated with and without exogenous IFN-β (10 ng/mL). Data presented as the mean of five replicates ± SD. E) Cell viability assessed by celltiter glo in CTRL or XRN1 knockout NCI-H747 cells treated with and without Ruxolitinib (1 μM). Data presented as the mean of five replicates ± SD. F) qPCR after Ruxolitinib (1 μM) treatment as in E. Values are normalized against RPLP0. Data presented as the mean of three technical replicates ± SD. G) Quantification of plate shown in 5F.

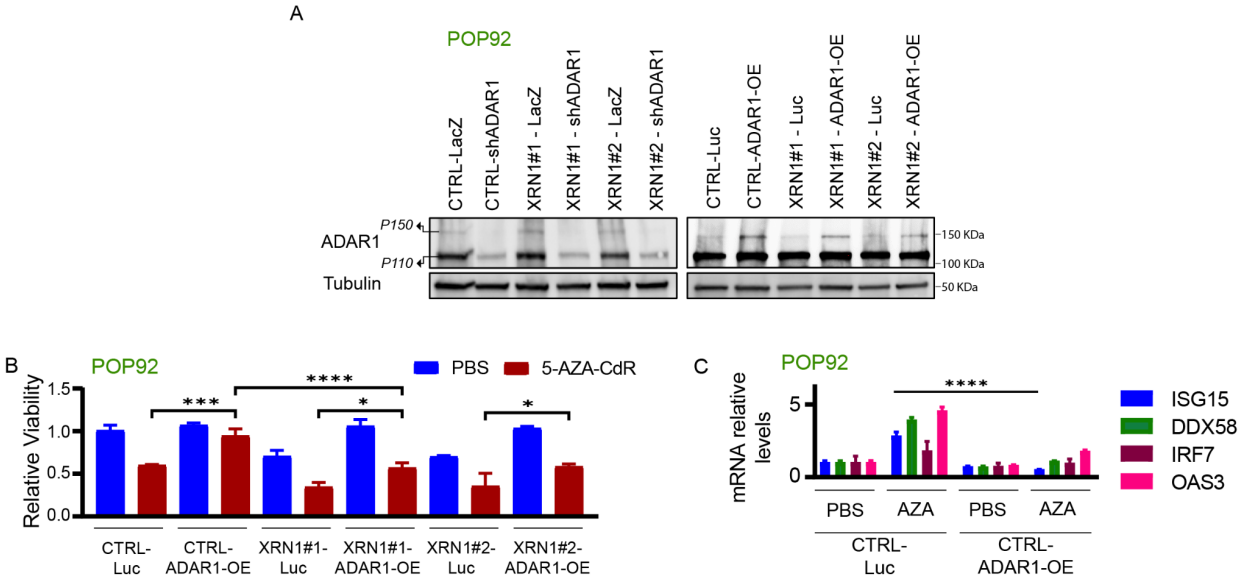

Figure S6. Depletion of XRN1 and over expression of ADAR1 in POP92 cells. A) Western blot of ADAR1 in POP92 cells with ADAR1 and XRN1 knockout and ADAR1 overexpression. Tubulin is loading control. sgRNA is used to knockout XRN1, #1 and #2 represents different sgRNA targeting XRN1. B) Extension of figure 6D including additional comparisons. Cell viability in POP92 cells with indicated knockout or overexpression determined with Cell Titer Glo assay. Data presented as the mean of triplicates ± SD. C) PCR of selected ISGs in POP92 cells with indicated overexpression of ADAR1. Values are normalized against RPLP0. Data presented as the mean of triplicates ± SD. Significance levels shown for ISG15, but are equal for the other genes.

References

1. Nusinow, D.P., Szpyt, J., Ghandi, M., Rose, C.M., McDonald, E.R., Kalocsay, M., Jané-Valbuena, J., Gelfand, E., Schweppe, D.K., Jedrychowski, M., et al. (2020). Quantitative Proteomics of the Cancer Cell Line Encyclopedia. Cell *180*, 387-402.e16. 10.1016/j.cell.2019.12.023.
2. Liu, H., Golji, J., Brodeur, L.K., Chung, F.S., Chen, J.T., deBeaumont, R.S., Bullock, C.P., Jones, M.D., Kerr, G., Li, L., et al. (2019). Tumor-derived IFN triggers chronic pathway agonism and sensitivity to ADAR loss. Nat. Med. *25*, 95–102. 10.1038/s41591-018-0302-5.
3. Liberzon, A., Birger, C., Thorvaldsdóttir, H., Ghandi, M., Mesirov, J.P., and Tamayo, P. (2015). The Molecular Signatures Database (MSigDB) hallmark gene set collection. Cell Syst. *1*, 417–425. 10.1016/j.cels.2015.12.004.